UNIVERSITY *of the*
WESTERN CAPE

Characterisation of the first $\frac{1}{2}^{+}$ excited state in ^{9}B and isospin symmetry breaking studies in $A = 9$ nuclei.

by

Mukwevho Ndinannyi Justice

A thesis submitted to
University of the Western Cape
for a
MASTERS degree

Department of Physics
Faculty of Natural Sciences
University of the Western Cape

March 11, 2019

Abstract

The ^{9}Be - ^{9}B isospin doublet carries fundamental significance for both nuclear structure and nuclear astrophysics studies. The first excited $\frac{1}{2}^+$ state in ^{9}Be is already well established. However, its isobaric analogue $\frac{1}{2}^+$ state in ^{9}B has not been unambigously determined yet. Theoretically, two popular descriptions of the ^{9}B nucleus either use a cluster model with two unbound α particles held together by a covalent proton or using the shell model, as a ^{8}Be core + proton in the sd shell. An experimental determination of the excitation energy of the first $\frac{1}{2}^+$ state in ^{9}B will provide valuable information in validating the theoretical model that adequately describes such light unbound nuclei. Further, it will also provide a robust test of mirror (isospin) symmetry violations via measurements of mirror energy differences in the doublet.

Although there have been several experimental attempts to characterize the first $\frac{1}{2}^+$ state in ^{9}B, several discrepancies still exist in reported values of the excitation energies. This thesis describes an experiment performed at iThemba LABS using the ^{9}Be(^{3}He, t)^{9}B reaction to address the above issue. As a byproduct, the thesis also describes an additional determination of the excitation energy of the second $J^\pi = \frac{1}{2}^-$, $T = \frac{3}{2}$ state in ^{9}B from the same experiment. This was performed in order to resolve a discrepancy related to the excitation energy of this state. The consequence of this measurement related to Isobaric Multiplet Mass Equation (IMME) for the excited $T = \frac{3}{2}$, $A = 9$ quartet is discussed briefly.

To my parents, Mukwevho Muvhango Edrick

and Mainganye Matevhutevhu Doris.

ACKNOWLEDGEMENTS

First of all, I would like to thank my supervisor Smarajit Triambak. Thank you for your support, for your infinite patience and guidance all these years. I would also like to thank the iThemba LABS K600 group, Retief Neveling, Luna Pellegri, Vicente Pesudo, Ricky Smit and Daniel José Marín-Lámbarri for their help during the experiment. A special thank you to my friend, colleague and office-mate, Bernadette Rebeiro, for her tireless assistance in many aspects of my research. She was like my co-supervisor. If it were not for her, I would not be where I am today. I would like to thank Mohamed Kamil for his friendship since day one, and express my sincere gratitude to my other office mates, Bhivek Singh and Jespere Ondze for their company and encouragement. I am grateful the administrative and teaching staff of the University of the Western Cape for all their help during my Honours coursework and Masters research. Lastly, I would like to thank my family for their love and support.

CONTENTS

LIST OF FIGURES

CHAPTER 1

BACKGROUND AND MOTIVATION

1.1 The atomic nucleus and isospin symmetry

The atomic nucleus is the small, heavy and central constituent of an atom and it consists of Z protons and N neutrons, which are called nucleons, The mass number for the nucleus is given by the sum of the neutron and proton numbers, $A = N + Z$. The nucleons (protons and neutrons) have the same intrinsic spin, $S = \frac{1}{2}$, and are fermions that obey Pauli's exclusion principle. Since the 1930's the analysis of pp and np scattering have consistently shown that after taking into account the Coulomb force, pp and np interactions were roughly equal in strength. It was therefore ascertained that the force between two nucleons is charge independent. This charge independence, together with the fact that protons and neutrons had nearly identical masses led Heisenberg to introduce a new quantum number called isospin. The projection of isospin, labelled the different charge states of a nucleon. In other words, the neutron and the proton can be represented as two states (projections) of the nucleon. This formalism is discussed in greater detail below.

1.1.1 Isospin formalism

The isospin formalism describing nucleons is equivalent to the description of spin-1/2 particles. As mentioned qualitatively previously, the proton and the neutron both have isospin $t = 1/2$ but with two different possible projections along the 3rd axis in isospin space (*i.e* $t_3 = +\frac{1}{2}$ for neutrons and $t_3 = -\frac{1}{2}$ for protons) as shown in Fig. 1.1. Thus, the t_3 quantum number is related to the charge of the nucleon.
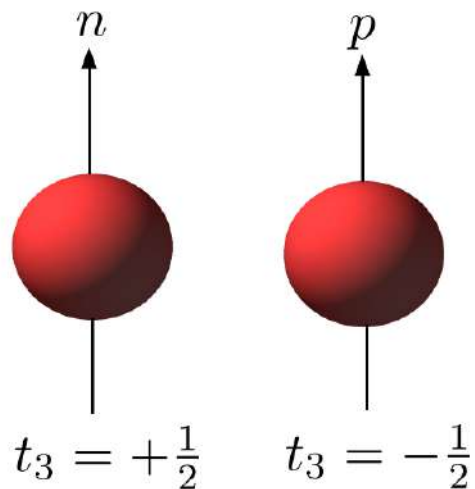
Figure 1.1: *Isospin 1/2 protons and neutrons, characterized by their projections along the 3rd axis in a 2-dimensional isospin space.*

The three components of the isospin vector satisfy similar commutation relations as those of spin-1/2 particles, given by

$$[t_1, t_2] = it_3, \ [t_2, t_3] = it_1, \ [t_3, t_1] = it_2. \tag{1.1}$$

Using the above convention, the charge q of a nucleon can be written as [1]

$$q = e(\frac{1}{2} - t_3). \tag{1.2}$$

With the help of Eq. (1.2), the total charge of a nucleus is obtained by summing over all nucleons, so that

$$Ze = \sum_{i=1}^{A} q_i = e(\frac{A}{2} - T_3). \tag{1.3}$$

The third component of the total nuclear isospin T is then simply

$$T_3 = \sum_{i=1}^{A} t_{3,i}. \tag{1.4}$$

From Eq. (1.3) it is easy to deduce that

$$T_3 = \frac{A}{2} - Z = \frac{(N - Z)}{2}. \tag{1.5}$$

For an atomic nucleus, the maximum value of T is $\frac{1}{2}A$ and the minimum value of T is $|T_3|$. Therefore the isospin of nuclei fall in the range [1]

$$\frac{1}{2}|N - Z| \leq T \leq \frac{1}{2}A. \tag{1.6}$$
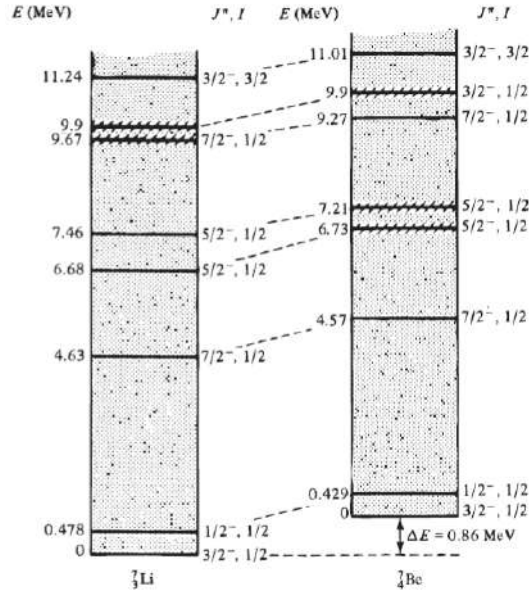
Figure 1.2: *Level scheme for $A = 7$ isobars. The energy levels in these nuclei are roughly identical. They shift relative to each other once electromagnetic corrections are taken into consideration. Figure taken from [1].*

Isospin is considered a good quantum number in the presence of hadronic forces alone and each quantum state of an atomic nucleus can be described by a value of isospin T. This near symmetry of isospin manifests itself as almost identical spectra in mirror pairs [2]. Therefore, even though the Coulomb force breaks this symmetry, the isospin quantum number can be used to identify isobaric analogue states in nuclei [2]. From Eq. (1.6), it is very clear that isospin singlets with $T = 0$ can only emerge in nuclides with $N = Z$. Such nuclides are called self-conjugate. Good examples of $T = 0$ nuclei are the ground states of the even-even nuclei such as ^{2}H, ^{4}He, ^{6}Li, ^{8}Be, ^{12}C, ^{14}N, ^{16}O, *etc.* Isospin doublets can only be found in mirror nuclides where $Z = (A \pm 1)/2$, as shown in Fig. 1.2. The ground states of isospin doublets (such as the mirror nuclei in Fig. 1.2) have isospin $T = 1/2$. An example of an isospin triplet is shown in Fig. 1.3, where the $T = 1$ triplet consists of the ground states of ^{14}C and ^{14}O with the first excited state of ^{14}N.
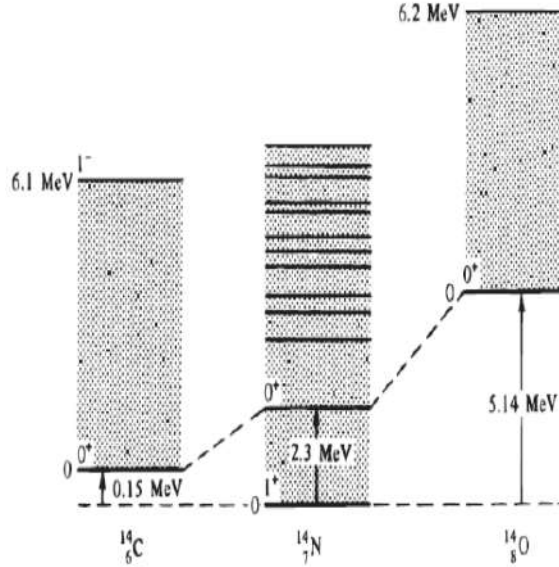
Figure 1.3: *Level scheme for A = 14 isobars. Note that the ground state of* ^{14}N *is a T = 0 singlet and the first excited state is a member of a T = 1 triplet. Figure taken from [1].*

1.2   Isospin symmetry breaking

The presence of an external electromagnetic field breaks the degeneracy of energy levels in atoms (the Stark and Zeeman effects [?]). Similarly, in atomic nuclei, charge-dependent interactions break isospin symmetry. This is shown in Fig. 1.2 and Fig. 1.3. The small differences between the analogue energy levels in nuclei is caused by this breaking of isospin symmetry. More explicitly, in the limit of perfect isospin symmetry, the isobaric analogue states (IAS) would have the same isospin T, spin-parity J^π and other properties. These IAS are characterised by different projections T_3 within the isobaric multiplet. The presence of purely charge independent hadronic forces results in a $(2T + 1)$-fold degeneracy for a given isobaric multiplet with isospin T,which would result the members of an isobaric multiplet having identical masses. The IAS shift relative to each other when $(2T + 1)$-fold degeneracy is lifted due to charge-dependent interactions. This is shown in Fig. 1.4, where the atomic

5

Zeeman effect is shown for comparison. The Zeeman effect occurs in the presence of an external magnetic field. The Coulomb displacement energy (CDE) in nuclei is defined as a measure of the isospin symmetry breaking in effective nuclear interactions and it is given by the differences between the excitation energy of the isobaric analogue states [3].

I describe the algebra of isospin symmetry breaking below.
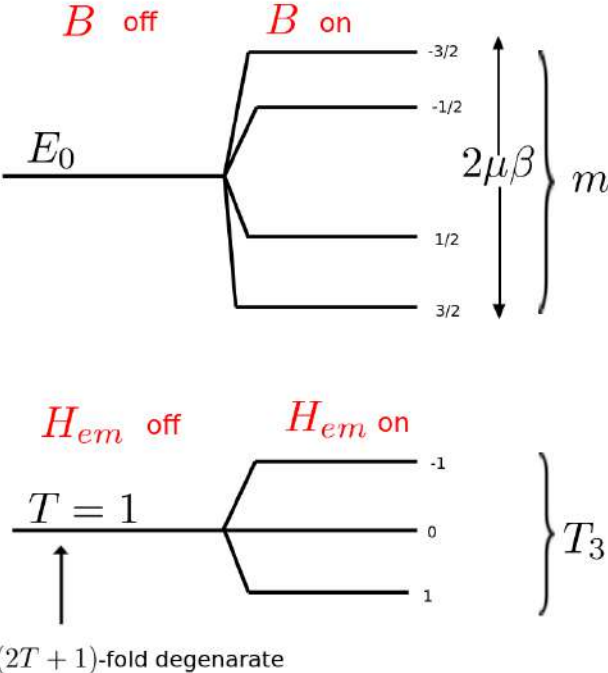
Figure 1.4: *Both spectra show the splitting of the degeneracy due to an external field. Top: Zeeman effect. Bottom: Isospin symmetry breaking.*

The charge independence of nuclear force requires that the total isospin T commutes with the hadronic Hamiltonian H_h (similar to angular momentum conservation and rotational invariance), such that

$$[H_h, T] = 0. \tag{1.7}$$

When an electromagnetic perturbation is added to the hadronic Hamiltonian, we get an

effective Hamiltonian

$$H = H_h + H_{em}. \tag{1.8}$$

The breaking of isospin symmetry results in $[H, T] \neq 0$. This implies that isospin is not a conserved quantity any more. However, since the charge q is always conserved, and it is related to T_3, we always have

$$[H, T_3] = 0. \tag{1.9}$$

The electromagnetic perturbation on the other hand can be written in terms of two-body Coulombic forces and the isospin operators as [4]

$$H_{em} = \sum_{i<j} (\frac{1}{2} - t_3^i).(\frac{1}{2} - t_3^j) \frac{e^2}{r_{ij}}, \tag{1.10}$$

where i and j label individual protons. H_{em} can be further separated as a sum of isoscalar, isovector and isotensor operator of rank 2,

$$H_{em} = H_{em}^0 + H_{em}^1 + H_{em}^2 \tag{1.11}$$

where,

$$
\begin{aligned}
H_{em}^0 &= \frac{1}{3} e^2 \sum_{i<j} (\frac{3}{4} + \vec{t}^i.\vec{t}^j) r_{ij}^{-1} \\
H_{em}^1 &= \frac{1}{2} e^2 \sum_{i<j} (t_3^i + t_3^j) r_{ij}^{-1} \\
H_{em}^2 &= \frac{1}{3} e^2 \sum_{i<j} (3 t_3^i t_3^j + \vec{t}^i.\vec{t}^j) r_{ij}^{-1}.
\end{aligned}
\tag{1.12}
$$

Using the Wigner-Eckart theorem, the T_3 dependencies can be factored out in such a way

that the reduced expectation value of the electromagnetic Hamiltonian is expressed as

$$E_{em}(A, T, T_3) = \sum_{k=0}^{2} (-1)^{T-T_3} \begin{pmatrix} T & k & T \\ T_3 & 0 & T_3 \end{pmatrix} \langle T || H_{em}^{(k)} || T \rangle. \tag{1.13}$$

This gives a quadratic relation in T_3 for the coulomb energies of the multiplet members which is written as

$$E_{em}(A, T, T_3) = E_{em}^{(0)}(A, T) - T_3 E_{em}^{(1)}(A, T) + (3T^2 - T(T+1)) E_{em}^{(2)}(A, T), \tag{1.14}$$

where the quantities $E_{em}^{(0)}$, $E_{em}^{(1)}$, and $E_{em}^{(2)}$ are the scalar, vector and tensor Coulomb energies, and are respectively given by

$$\begin{aligned} E_{em}^{(0)} &= \langle T || H_{em}^0 || T \rangle \\ E_{em}^{(1)} &= \frac{-1}{\sqrt{T(T+1)}} \langle T || H_{em}^1 || T \rangle \\ E_{em}^{(2)} &= \frac{-1}{\sqrt{T(T+1)(2T-1)(2T+3)}} \langle T || H_{em}^2 || T \rangle. \end{aligned} \tag{1.15}$$

This results in a relation for masses of an isobaric multiplet members [4]

$$M(A, T, T_3) = \frac{1}{2}(m_n + m_H)A + (m_n - m_H)T_3 + \langle TT_3 | H_0 | TT_3 \rangle + \langle TT_3 | H_1 | TT_3 \rangle + E_{em}(A, T, T_3). \tag{1.16}$$

Therefore, using Eq. (1.14), Eq. (1.15) and Eq. (1.16), it is sufficient to express the masses of an isobaric multiplet using the quadratic form

$$M(A, T, T_3) = a(A, T) + b(A, t)T_3 + c(A, T)T_3^2 \tag{1.17}$$

which is called the isobaric multiplet mass equation (IMME). The a, b and c coefficients are related to diagonal reduced matrix elements of the charge-dependent part of the total

Hamiltonian. These coefficients incorparate all the wavefunction information, and can either be calculated or obtained experimentally from a quadratic fit to the measured mass excesses of the multiplet members. Since this model uses first order perturbation theory to relate the masses of the IAS, it is expected that the above quadratic form of the IMME breaks down when first order perturbation theory is not enough to satisfactorily describe the data. Such a breakdown can occur due to either largely differing wavefunctions in the IAS due to mixing with other isospin states or due to the weakly bound nature of some of the IAS which would couple with the unbound particle continuum [4]. In such a scenario, the IMME would require additional cubic (dT_3^3) or quartic (eT_3^4) terms.

1.2.1   Isospin mixing of two nuclear states

Consider two initial nuclear states represented by $|\phi_1\rangle$ and $|\phi_2\rangle$. Assume these states have the same spin and parity but have different isospin. If they have energies eigenvalues E_1 and E_2, that are separated by an energy difference ΔE_u, as shown in Fig. 1.5, then the actual states involved that describe nuclear properties are not the 'pure' states $|\phi_1\rangle$ and $|\phi_2\rangle$. Instead, they are admixtures of the two configurations, represented by $|\psi_1\rangle$ and $|\psi_2\rangle$. This is due to an effective residual two-body interaction between the nucleons, which we denote by V. The energy eigenvalues and eigenvectors can be obtained to the lowest-order in perturbation theory by diagonalising the 2×2 matrix [5]

$$\begin{pmatrix} E_1 & V \\ V & E_2 \end{pmatrix} \tag{1.18}$$

where the isospin mixing matrix element is given by $\langle\phi_1|V|\phi_2\rangle$.
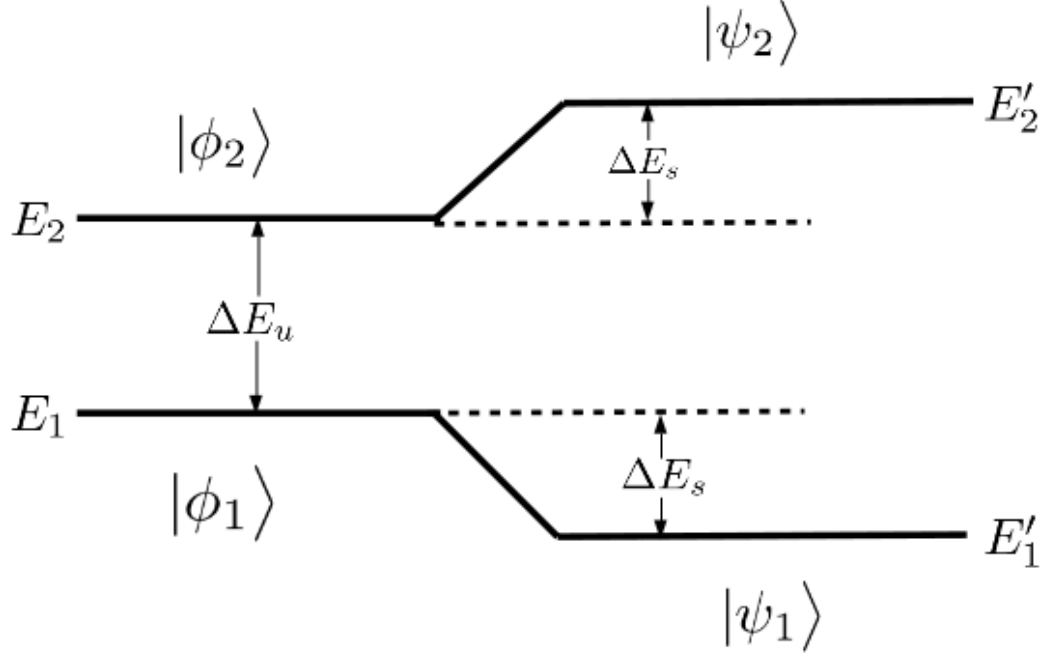
Figure 1.5: *The repulsion of energy levels in a nucleus due to two-state isospin mixing.*

The extent of isospin mixing relies on both the ΔE_u and the magnitude of the matrix element $\langle \phi_1 | V | \phi_2 \rangle$. A large energy spacing ΔE_u in Fig. 1.5 reduces the effect of isospin mixing and vice versa. On defining a ratio λ, it can be easily shown

$$\lambda = \frac{\Delta E_u}{\langle \phi_1 | V | \phi_2 \rangle}, \tag{1.19}$$

that the perturbed energies in terms of the unperturbed levels E_1 and E_2 takes the form [5]

$$\begin{aligned} E'_1, E'_2 &= \frac{1}{2}(E_1 + E_2) \pm \frac{1}{2}\sqrt{(E_2 - E_1)^2 + 4\langle\phi_1|V|\phi_2\rangle^2} \\ &= \frac{1}{2}(E_1 + E_2) \pm \frac{\Delta E_u}{2}\sqrt{1 + \frac{4\langle\phi_1|V|\phi_2\rangle^2}{\Delta E_u^2}} \\ &= \frac{1}{2}(E_1 + E_2) \pm \frac{\Delta E_u}{2}\sqrt{1 + \frac{4}{\lambda^2}}. \end{aligned} \tag{1.20}$$

Therefore, final energy difference is simply

$$E'_2 - E'_1 = \Delta E_u \sqrt{1 + \frac{4}{\lambda^2}}. \tag{1.21}$$

It can be also trivially shown that each energy eigenvalue shifts by an amount

$$|\Delta E_s| = |E'_2 - E_2| = |E'_1 - E_1| = \frac{\Delta E_u}{2}\left[\sqrt{1 + \frac{4}{\lambda^2}} - 1\right], \tag{1.22}$$

as a result of the perturbation. The admixed wave functions take the final form

$$\begin{aligned} \psi'_1 &= \alpha\phi_1 + \beta\phi_2 \\ \psi'_2 &= \beta\phi_1 + \alpha\phi_2, \end{aligned} \tag{1.23}$$

where the probability amplitudes α and β are such that $\alpha^2 + \beta^2 = 1$. The probability amplitude β can be expressed in terms of R, so that

$$\beta = \frac{1}{\left\{1 + \left[\lambda/2 + \sqrt{1 + \lambda^2/4}\right]^2\right\}^{\frac{1}{2}}}. \tag{1.24}$$

1.3 Coulomb Energy differences & the Thomas-Ehrman shift

Coulomb displacement energies between isobaric analogue states provide useful information to better understand isospin symmetry breaking and structure of atomic nuclei. Many investigations have already been carried out over the years, in which comparisons have been made between theory and experiment over a wide range of nuclei [6]. It has been observed that just incorporating the Coulomb repulsion between protons gives a reasonable approximation for the energy differences of mirror nuclei. This Coulomb energy difference in mirror nuclei is given by [7]

$$\Delta E_c = B(N+1, Z) - B(N, Z+1) \tag{1.25}$$

where $B(N, Z)$ is the binding energy for a nucleus with N neutrons and Z protons. In 1950 Thomas [8] and Ehrman [9] suggested that the presence of the Coulomb force for protons causes a distortion in loosely bound proton wave functions compared to the neutron wave functions, such that the CDE's in IAS get affected further. Such Thomas-Ehrman effects occur due to the radial expansion of the proton wave functions on account of the coupling of these states with the continuum. These are discussed in greater detail in the next section.

1.4 The nuclear shell model

An important idea in providing a simplified description of the complex details of nuclear structure was provided by the atomic shell model. Fig. 1.6 shows a plot of 2 proton and 2 neutron separation energies for several nuclei against nucleon number. This pattern is remarkably similar to those for ionisation energies in atoms: $i.e$ a continous increase with N or Z except for a few sharp drops that occur at specific neutron and proton numbers, called the magic numbers (2, 8, 20, 28, 50, 82, 126). These numbers represent the effects of

filled major shells, which is similar to the atomic model, where atomic shells are filled with electrons in accordance to Pauli exclusion principle. In the atomic shell model, an inert core of filled shells together with the valence electrons determine atomic properties. The potential felt by the electrons in atoms is created by the Coulomb field of the nucleus. Similarly, in the nuclear shell model, orbits are filled with nucleons but there does not exist any external potential. The fundamental difference from the atomic model is that the mean field felt by the nucleons is created by the nucleons themselves.
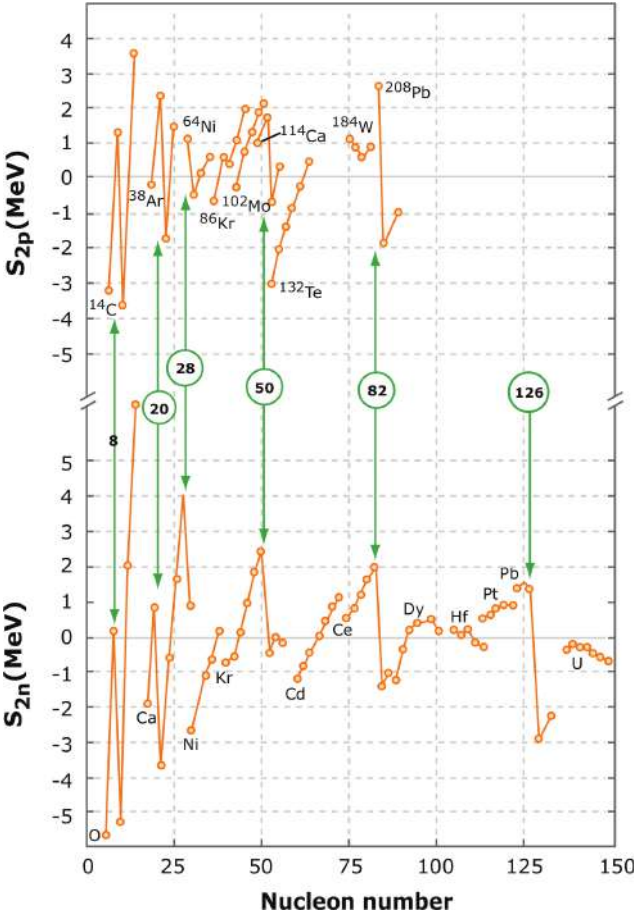
Figure 1.6: *A plot of proton-proton (top) and neutron-neutron (bottom) separation energies against Z (top) and N (bottom). The sudden change appears at the magic numbers (green-circled numbers). Figure taken from [10] (adapted from Ref. [11]).*

The nuclear Hamiltonian in the *independent* particle shell model is given by the sum of a

residual interaction $\hat{V}$ and Hamiltonian $\hat{H}_0$ [12]

$$\hat{H} = \hat{H}_0 + \hat{V}, \tag{1.26}$$

where $\hat{H}_0$ is the summation of single-particle Hamiltonian,

$$\hat{H}_0 = \sum_{i=1}^{A} \hat{h}_i. \tag{1.27}$$

This Hamiltonian corresponds to a system of nucleons moving independently in a single-particle potential, so that $\hat{h}_i$ controls the motion of the ith nucleon. A simple single particle Hamiltonian $\hat{h}_i$ can be expressed as

$$\hat{h}_i = \frac{\hat{p}_i^2}{2M} + U(r_i) \tag{1.28}$$

where $\hat{p}_i = -i\hbar \vec{\nabla}_i$ is the nucleon momentum, M is the mass of a nucleon, r_i is the radial coordinate of the ith nucleon and $U(r_i)$ is the single-particle potential. The potential under which the nucleons move is the key to the model. The first step in developing shell model is to consider two potentials : the infinite square well and the harmonic oscillator. The 3-dimensional infinite square well potential is

$$U(r) = \begin{cases} -V_0, & \text{if } r < R \\ \infty, & \text{if } r \geq R, \end{cases} \tag{1.29}$$

while the spherical harmonic oscillator potential is

$$U(r) = \frac{1}{2}M\omega^2 r^2, \tag{1.30}$$

where ω is the angular momentum. Both these potentials can be used to solve single-nucleon

14

wave functions analytically. The infinite square well potential yields the magic numbers $2, 8, 18, 20, 34, 40, 58, 68, 90, 92$ and only the first few agree with experiment. It also has a few other disturbing limitations. Firstly, to separate a nucleon from a nucleus, an infinite amount of energy must be provided. Furthermore a realistic nuclear potential does not have sharp edges unlike the infinite square well but falls smoothly to zero beyond the mean nuclear radius $\bar{R}$, closely approximating the nuclear charge and matter distributions. The harmonic oscillator potential is smooth and yields reasonable analytical solutions of the Schrödinger equation. However, despite this smooth behaviour, the potential has other several limitations. The potential goes to infinity when r increases indefinitely, again implying infinite separation energies similar to the square well. Furthermore, due to rotational symmetry in 3-dimensions, the harmonic oscillator potential gives degenerate solutions [13] for different ℓ-values of orbital angular momentum. And finally, although it works satisfactorily in reproducing low-lying energies and several magic numbers, differences start to show up as the energies and nucleon numbers increase. Therefore an alternative to both these potential is the Woods-Saxon potential

$$V(r) = \frac{-V_0}{1 + exp(r - R)/a}, \tag{1.31}$$

where R is the range of the potential, and a and V_0 denote skin thickness and well depth respectively. These parameters can be adjusted to give the proper separation energies and the energy levels shown in Fig. 1.7. The Wood-Saxon potential also removes ℓ degeneracies of the major shells because the particles with the higher ℓ-values are on average at a larger distance from the centre of the well than the particles with a lower ℓ-values [14]. One of the disadvantages of the Woods-Saxon potential is that single-particle wave functions can only be computed numerically. An alternative is to add a $D\ell^2$ term, with $D < 0$ to the single particle Hamiltonian for the spherical harmonic oscillator potential.

$$\hat{H} = -\frac{\hbar^2 \nabla^2}{2M} + \frac{1}{2} M \omega^2 \mathbf{r} + D\ell^2. \tag{1.32}$$

15

This breaks the ℓ degeneracy and lowers the energy of a state with orbital angular momentum ℓ by an amount that is proportional to $\ell(\ell + 1)$ [12]. However despite addressing the most obvious problems, these shell model potentials still do not reproduce all the experimentally observed magic numbers and shell gaps. To improve the situation further, Mayer, Haxel, Suess and Jensen proposed to add a spin-orbit term in the potential. The spin-orbit term is simply [11]

$$V_{so}(r) = V_{\ell s}(r)\vec{\ell} \cdot \vec{s}, \tag{1.33}$$

where $\vec{\ell}$ and $\vec{s}$ denote the orbital angular momentum and the intrinsic spin of the nucleon respectively. The $\vec{\ell} \cdot \vec{s}$ factor causes the reordering of the single particle levels in the following manner. In the presence of spin-orbit interaction, states are labelled with the total angular momentum $\vec{j} = \vec{\ell} + \vec{s}$. A single nucleon has $s = \frac{1}{2}$, with possible values of the total angular momentum quantum number $\ell + \frac{1}{2}$ or $\ell - \frac{1}{2}$. Therefore, the expectation value of $\vec{\ell} \cdot \vec{s}$ is given by the following expression

$$< \vec{\ell} \cdot \vec{s} >= \frac{1}{2}[j(j + 1) - \ell(\ell + 1) - s(s + 1)]\hbar^2. \tag{1.34}$$

This causes a reordering of the levels as can be shown in the following example. Consider the $0f$ level in Fig. 1.7. The possible values of the total angular momentum for this state are $j = \ell \pm \frac{1}{2} = 7/2$ or $5/2$. This splits the level into both $0f_{5/2}$ and $0f_{7/2}$ states. Each level has $(2j + 1)$ degeneracy which arises from the m_j substates. The $0f_{5/2}$ and $0f_{7/2}$ states are called a spin orbit pair or doublet. These states are separated by an energy that is proportional to the $< \vec{\ell} \cdot \vec{s} >$ value for each state. When ℓ increases, the energy splitting also increases. The effect of this splitting is shown on the extreme right of Fig. 1.7.

16
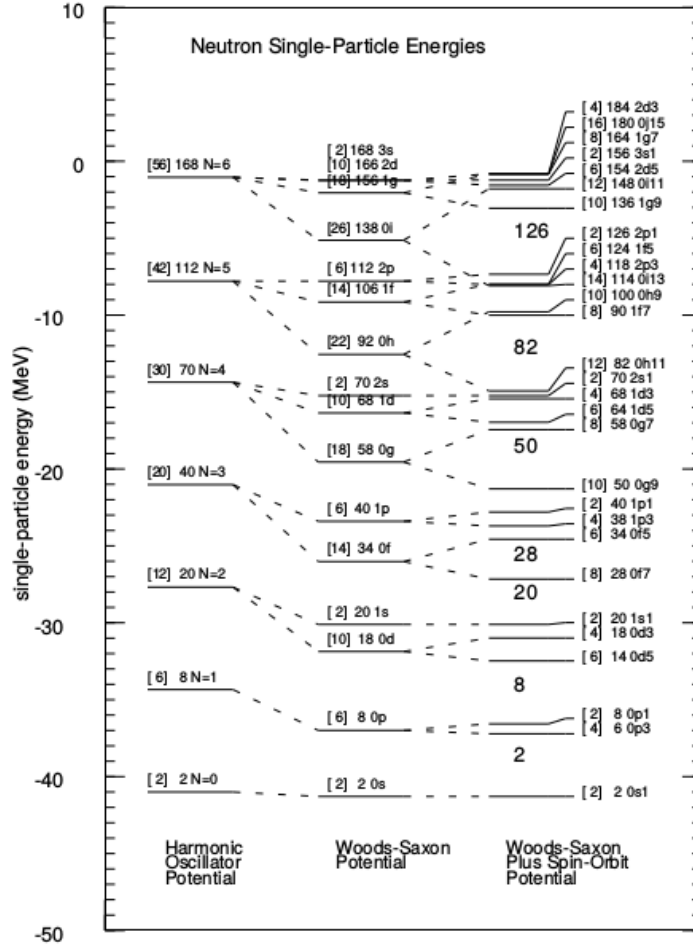
Figure 1.7: *Diagram showing the results of adding the spin-orbit interaction to a potential. Here the spin-orbit term was added to the Wood-Saxon, which results in a splitting of the states with $\ell > 0$. Taken from [15].*

We now return to the discussion of Thomas-Ehrman shifts in the context of the shell model. As an example, on comparing the energy spacings between the $\frac{1}{2}^-$ ground state and the excited $\frac{1}{2}^+$ levels in the ^{13}N $-^{13}$C mirror pair, it was found that the energy gap in ^{13}N was 720 keV smaller than in ^{13}C. The levels can be described as a single-particle $0p_{1/2}$ neutron state and a $1s_{1/2}$ proton state respectively. Because the centrifugal barrier is absent in the $1s_{1/2}$ orbit ($\ell = 0$), making the proton less bound, it was apparent that the Thomas-

Ehrman (T-E) shift would be larger for the $1s_{1/2}$ orbit compared to the $0p_{1/2}$ orbit. Thus, as the proton wave function extends further, the T-E effect can be explained to emerge due to mismatch between the wave functions for the odd nucleon. However, it should be noted that not all of the 720 keV energy difference in the above example is because of the Thomas-Ehrman effect. About 600 keV of the energy difference is simply because of the Coulomb displacement energy. It is now well understood and accepted that the Thomas-Ehrman shift contribution begins to cause appreciable effects at energies near the particle separation threshold [16].

1.5 Motivation for this work.

1.5.1 Energy level spectra for the $A = 9$ mirror pair

The $A = 9$ mirror pair, ^{9}Be and ^{9}B, plays an important role in understanding the structure of light unbound nuclei and the role of Coulomb displacement energies in mirror nuclei. Such light nuclei are interesting due to several reasons. They have been at the forefront of intense experimental and theoretical activity considering recent advances in *ab initio* based calculations [17]. Additionally there have been a lot of interest in studying the clustering properties of these nuclei, using microscopic cluster models [18]. Therefore, experimental information regarding the structure of these nuclei are important in order to address several open questions that are of current interest.
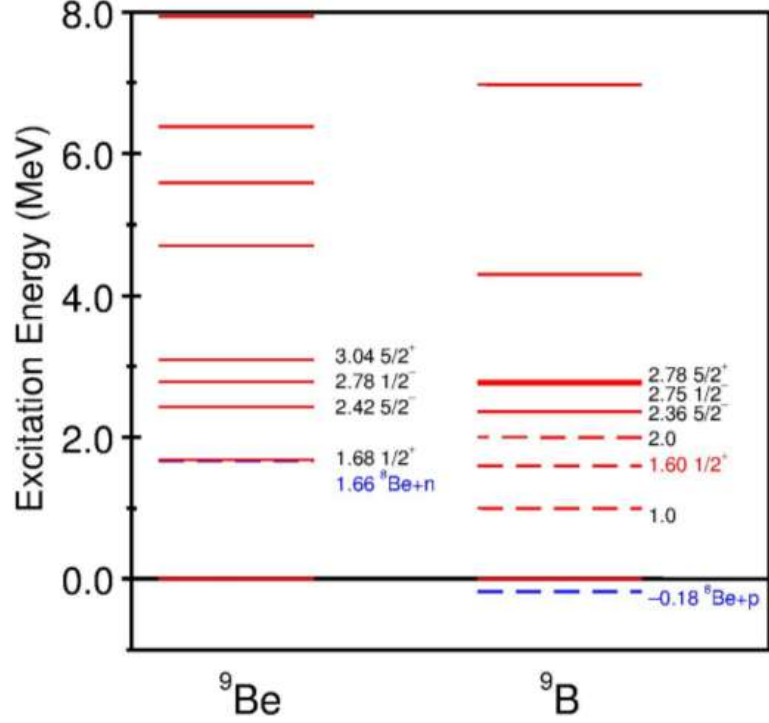
Figure 1.8: *The energy levels of* ^{9}Be *and* ^{9}B.

Fig 1.8 shows the nominal energy levels of ^{9}Be and ^{9}B for comparison, where the ground state is taken as zero. As can be seen, the ground state of ^{9}B itself is unbound to proton emission. Many experiments have already been performed on both these nuclei and several states below 3.1 MeV have been successfully matched with their mirror partners [19]: ^{9}Be($\frac{3}{2}^-$, *g.s.*) $-$ ^{9}B($\frac{3}{2}^-$, *g.s.*), ^{9}Be($\frac{5}{2}^-$, 2.43) $-^9$B($\frac{5}{2}^-$, 2.36), ^{9}Be($\frac{5}{2}^+$, 3.05) $-^9$B($\frac{5}{2}^+$, 2.79). Over the past several decades there have also been extensive theoretical and experimental efforts directed towards predicting and observing the first excited $\frac{1}{2}^+$ state in ^{9}B. However, although the unbound first excited $\frac{1}{2}^+$ state of ^{9}Be at 1.68 MeV has been known for many years [20], knowledge of the first excited $\frac{1}{2}^+$ state in ^{9}B has been inconclusive. This is mainly because the state is very broad and is present amongst much more intensely populated peaks that also have large widths. I summarize current knowledge of this state in the next chapter, where I describe also some of the theoretical models used to describe the $A = 9$ isospin doublet.

1.5.2 Isobaric Multiplet Mass Equation (IMME) for the $A = 9$, $T = 3/2$ quartet

The energy levels in $A = 9$ nuclei, particularly ^{9}B and ^{9}Be are important in elucidating other isospin symmetry properties that are relevant for studies of nuclear structure. In the past there have been several experimental tests carried out to look for deviations from the quadratic form of the IMME shown in Eq. (1.17). Any breakdown of the IMME would require the inclusion of a T_3^3 cubic term or a T_3^4 quartic term. Furthermore, the IMME breakdown would indicate many possibilities like the requirement of three-body forces, strong isospin mixing with other states that have the same spin/parity as the IAS, or the need for a higher-order perturbation theory to describe mass splittings [4]. However it is generally observed that the quadratic form of the IMME holds very well for most nuclei up to $A \sim 40$ [21]. Significant deviations are expected in light nuclei with particle unbound states (such as ^{9}B) [4]. The breakdown would occur because the wave functions of the IAS would expand for the proton rich members of the multiplet due to their coupling with the particle continuum (Thomas-Ehrman effects) [4]. In this regard, the $A = 7$, $A = 8$, and $A = 9$ multiplets have been studied extensively since many of the isobaric analog states in these nuclei have large widths that would contribute to a violation of the IMME [4]. Recent measurements at radioactive ion beam facilities have carried out some of the most stringent IMME tests in these multiplets to further investigate such isospin non-conserving effects in light nuclei; especially the $A = 9$, $T = 3/2$ quartet [22] and $A = 8$, $T = 2$ quintet [23]. The most recent compilation [21] of $A = 9$ ground state masses and excitation energies shows that its lowest $T = 3/2$ quartet requires a dT_3^3 cubic term with $d = 6.7 \pm 1.5$ keV, for a good fit to the data [21]. This value agrees with the theoretical predictions ($d \sim 4$ keV) of Bertsch and Kahana, who used a combination of three-body second-order Coulomb and other charge-dependent nuclear interactions [24]. The enhanced d coefficient is natural consequence in their calculations

because of the reduced binding of the last $p_{3/2}$ proton in ^{9}C.
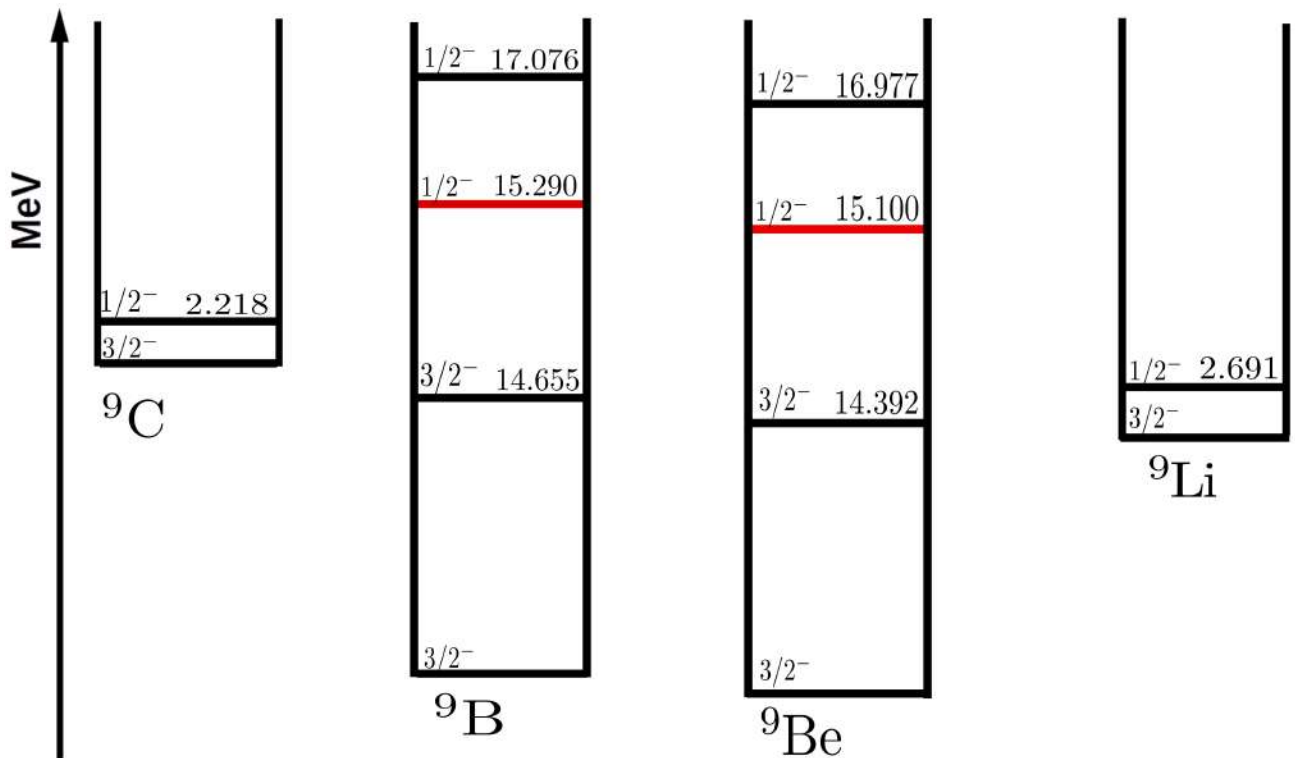
Figure 1.9: *The $A = 9$, $T = 3/2$ quartet. The ground states are expressed in terms of mass excesses, $\Delta = M - A$. Potential admixed states are shown in red.*

In contradiction with the explanation of Bertsch and Kahana, recent shell model calculations [22] have attributed the d coefficient in the first $A = 9$ quartet to isospin mixing with nearby $T = 1/2$ states in the $T_3 = \pm 1/2$ members of the multiplet. The admixed states (of undetermined spin and parity) occur at excitation energies of 15100 ± 50 and 15290 ± 40 keV for ^{9}Be and ^{9}B respectively [22, 25], shown in Fig. 1.9. The shell model prediction for the cubic coefficient with a PJT Hamiltonian [26, 27] was found to be in excellent agreement with the experimental value [22]. The shell model argument relied on the following: If the IMME breakdown were indeed due to particle continuum coupling effects as suggested by

Bertsch and Kahana, then the breakdown should be far worse of the second $T = 3/2$ quartet in $A = 9$ shown in Fig. 1.9. This is because the IAS for both ^{9}B and ^{9}C in the excited state quartets are particle unbound (*i.e* the proton separation energies are much smaller) [25]. However, a fit to the masses for the most precise available data in the excited quartet yields $d = 3.2 \pm 2.9$ keV, which is consistent with zero and therefore supports the isospin-mixing interpretation of Ref [22]. This assumption comes under question if one takes into account a recent determination of the excitation energy of the second $T = 3/2$ state in ^{9}B [28]. The authors of Ref [28] reported the energy of the state to be 16990 ± 30 keV by measuring the energies of the break up particles from the ^{9}B $\rightarrow p + ^8$Be(2α) decay channel. This value disagrees with the previous precise determination of $E_x = 17076 \pm 4$ keV from an older ^{11}B(p,t) measurement [29]. On using the result from Ref [28] a cubic IMME fit gives a significant value of $d = -60 \pm 15$ keV, which still does not rule out the explanation provided by Bertsch and Kahana. To address this problem, we performed a remeasurement of the energy of the second $J^\pi = 1/2^-$, $T = 3/2$ state in ^{9}B using the ^{9}Be$(^3$He$, t)$ reaction. Our result disagrees with the latest determination.

CHAPTER 2

THEORETICAL MODELS DESCRIBING THE ^{9}B NUCLEUS

2.1 The single-particle potential model

Since there were indications that the first $\frac{1}{2}^+$ state in ^{9}Be was a single-particle state in s-wave ($\ell = 0$) scattering, mirror symmetry requires that the first $\frac{1}{2}^+$ state in ^{9}B have similar properties. However, if it were indeed a single-particle $2s_{1/2}$ state, its excitation energy would be lowered relative to its IAS in ^{9}Be due to the Thomas-Ehrman shift [30]. In an early analysis Sherr and Bertsch characterized the first $\frac{1}{2}^+$ in ^{9}B state using a simple Woods-Saxon potential that was used to compute the widths and energies of mirror states in both mirror nuclei. In order to do this, they first adjusted the depth of the potential to predict the broad $s_{1/2}$ and $p_{1/2}$ resonances for unbound states in other light nuclei that was compared with experimentally available data. Since reaction data had already showed a well defined $\frac{1}{2}^+$ state in ^{9}Be, Sherr and Bertsch defined the level to be the energy at which the amplitude

$$C(E) = \int \Psi(r) r \phi_0(r) r^2 dr, \tag{2.1}$$

was maximal. In the above, $\phi_0(r)$ is the bound $p_{3/2}$ wave function for the ^{9}Be ground state and $|C(E)|^2$ is proportional to the probability of creating a continuum state from the ground state

with the operator $\imath r$. As shown in Fig. 2.1(a), a comparison of the predicted line shape for

the $^9\mathrm{Be}(\gamma, n)$ reaction with the experimental result of Fujishiro *et al* [31] showed a reasonable

agreement using this prescription, assuming a well depth of $V_0 = 56.3$ MeV. A similar analysis

was performed to calculate the lineshape for the excitation of the $^9\mathrm{B}(\frac{1}{2}^+)$ excited state from

its ground state. This yielded a theoretically predicted value of $E_x(\frac{1}{2}^+) = 0.93$ MeV, with

a width of 1.4 MeV (see Fig. 2.1(b)), indicating that the Thomas-Ehrman shift persisted

even when s-wave neutron became unbound. Table 2.1 shows a comparison of theory versus

experiment from this work.
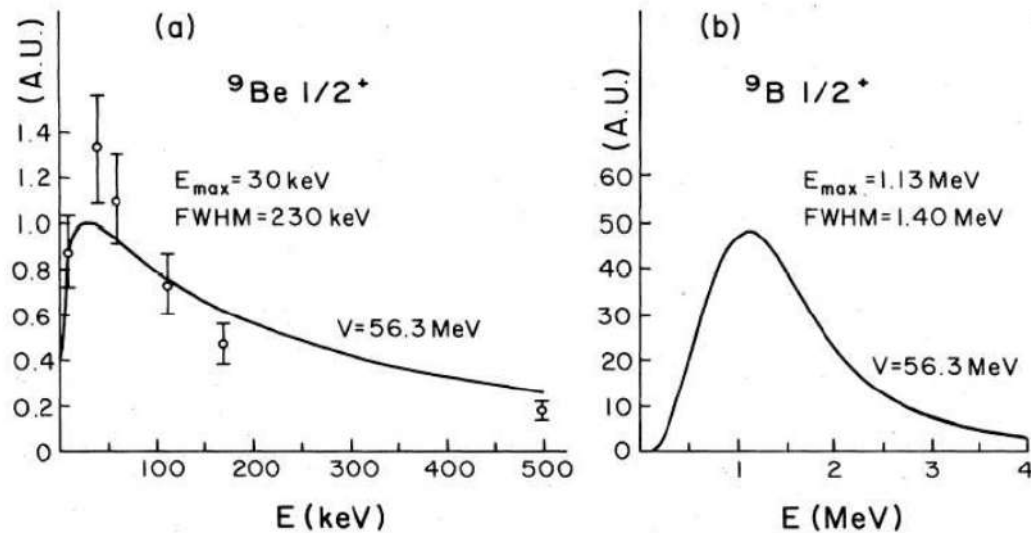
Figure 2.1: *Calculated lineshapes for the gs $\to 1/2^+$ excitations in the $A = 9$ mirror pair. Figure taken from [30].*

Table 2.1: *Single-particle potential model computations of excitation energies (E_x) andf total widths (Γ), in comparison with experimental values. Figure taken from [30] (adapted from [32]).*

	^9Be		^9B		
	E_x	Γ	E_x	Γ	V_0
	(MeV)	(keV)	(MeV)	(keV)	(MeV)
$\frac{3}{2}^-$(exp.)	0	-	0	0.5	−
$\frac{3}{2}^-$(calc.)	0.10	-	0	1.3	41.5
$\frac{1}{2}^-$(exp.)	1.69	150	1.65	(~ 1000)	−
$\frac{1}{2}^-$(calc.)	1.70	230	0.93	1400	56.3
$\frac{1}{2}^+$(exp.)	2.78	1080	(2.6)	~ 2400	−
$\frac{1}{2}^+$(calc.)	2.80	~ 1300	2.40	~ 2400	28.4
$\frac{5}{2}^+$(exp.)	3.05	280	2.79	550	−
$\frac{5}{2}^+$(calc.)	2.95	180	2.81	580	73.6

In 2004 Sherr and Fortune [33] revisited the calculations by adding nucleon coupling to core levels other than just the ground state in ^{8}B, and further including ^{5}He and ^{5}Li cores as well. This work was followed by an analysis of the second 0^+ state in the ^{10}Be-^{10}B doublet, which was found to have an almost pure $(sd)^2$ configuration. It was found that on coupling a $2s_{1/2}$ neutron to the $\frac{1}{2}^+$ state in ^{9}Be and varying the depth of the potential well, the excitation energy of the 0_2^+ state in ^{10}Be could be reproduced. A similar analysis was performed using a $1d_{5/2}$ neutron and the $5/2^+$ state in ^{9}Be. Assuming that the 0_2^+ state in ^{10}Be contains equal parts of both ^{9}Be $+ p$ and ^{9}B $+ n$ amplitudes, since the $5/2^+$ state in ^{9}Be is well known, the $2s_{1/2}$ and $1d_{5/2}$ admixtures in the 0_2^+ state in ^{10}B determined the excitation energy of the first $\frac{1}{2}^+$ state in ^{9}B [34]. This was found to be at a higher value than the older result shown in Fig. 2.1, at $E_x = 1.3 \pm 0.1$ MeV.

2.2   Microscopic Cluster Model

The microscopic cluster model was developed to provide a description of bound, resonant and scattering states in a unified manner. For example, it was used to describe radiative capture rates and electromagnetic transition strengths in light nuclei using the general-coordinate method (GCM) [35, 36]. The advantage of this model is that it does not contain any free parameters and reproduces elastic scattering cross-sections as well as electromagnetic properties of light nuclei reasonably well. Furthermore, it provides fairly accurate level scheme predictions, such as the Coulomb energy differences between mirror nuclei [37]. In 1989, Descouvemont employed the GCM and a microscopic-three cluster model to describe the ^{9}Be - ^{9}B mirror pair [38]. By this time it was well established that the ^{9}Be and ^{9}B low-lying states can be described as $n + {}^8$Be and $p + {}^8$Be respectively, with ^{8}Be being perfectly modelled by an $\alpha + \alpha$ cluster structure. Since these nuclei involve a cluster with an additional spin $\frac{1}{2}$ nucleon, this requires a spin-orbit force and additional angular momentum couplings to be introduced. The total microscopic wave function of the system in the GCM formalism with spin J and parity π is given by [38]:

$$\Psi^{JM\pi} = \sum_{lLI} \mathcal{A}[Y_l(\hat{\rho}) \otimes [Y_L(\hat{\rho}\prime) \otimes \phi_n]^I]^{JM} \phi_\alpha \phi_\alpha G_{lLI}^{J\pi}(\rho, \rho\prime), \qquad (2.2)$$

where $\mathcal{A}$ is an antisymmetrisor operator, and ϕ_α and ϕ_n are the internal wave functions of the alpha particle and of the orbiting nucleon. $G_{lLI}^{J\pi}$ is a radial wave function depending on the relative co-ordinates $\rho\prime$ between the α particles and ρ between the nucleon and ^{8}Be centre-of-mass. The orbital momentum of the ^{8}Be cluster is L while that of the external nucleon around the ^{8}Be core is given by ℓ. I is the channel spin. Fig. 2.2 shows a depiction of the two nuclei using the three cluster model. In many of these models the ^{9}Be(^{9}B) nuclei have been described as Borromean systems, where the nuclei are described (in a manner similar to the H_2^+ molecule) in which two unbound α-particles are held together by a covalent σ-type
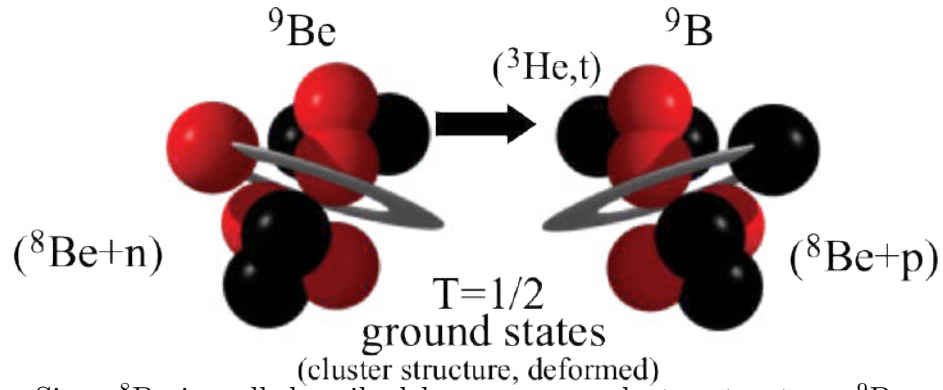
Figure 2.2: Since ^{8}Be is well described by an $\alpha + \alpha$ cluster structure, ^{9}Be and ^{9}B nuclei can be described in a Borromean model as $n +^8$ Be and $p +^8$ Be respectively. Figure taken from [39].

neutron (proton) [18]. The GCM cluster model prediction for the energy of the first $\frac{1}{2}^+$ in ^{9}B was found to be 1.35 MeV [38], in agreement with the single-particle potential model.

2.3   The R-Matrix Model

The **R**-matrix theory was first proposed by Wigner and Eisenbud in 1947 [40]. In the most general formulation, since the algebra for describing a set of states and their associated cross sections is very difficult, it is more convenient in this model to introduce a set of intermediary quantities called L, Ω, and R matrices. The first two matrices are diagonal and explain any long-range non-polarizing interactions between separated nuclei. The **R**-matrix is non diagonal and take into account the effects of nucleon-nucleon interactions in compound nuclei as well as those that can be described as separated pairs [41]. Wigner and Eisenbud showed that the energy dependence of any element of **R** can be expressed in the form [40] :

$$R_{cc'}(E) = \sum_\lambda \frac{\gamma_{\lambda c}\gamma_{\lambda c'}}{E_\lambda - E}$$ (2.3)

27

where λ determines the members of a complete set of states. The $\gamma_{\lambda c}$ are called the "reduced width amplitudes". The E_λ are the energy eigenvalues of the states labelled as λ. Barker *et al* [42] used the **R**-matrix theory to characterize states in light nuclei especially the ^{9}B nucleus. The formation assumed a reaction of the type A(a, b)B, in which the nucleus B is formed in a state that is unstable to particle emission. The cross section for the reaction, given the energy distribution of the particle b, can be represented in terms of a density-of-states function $\rho(E_B)$ for the nucleus B. This gives the probability of formation for the nucleus B with an excitation energy E_B. Barker *et al* used density of states functions for s-wave proton and neutron emission, together with experimental data from ^{9}Be(γ, n), ^{9}Be$(p, p\prime) \rightarrow n+^8Be(2\alpha)$ and ^{9}B(p, n) reactions to characterise low-lying particle unbound states in the ^{9}Be/^{9}B doublet. This work was followed by a more focused investigation of the first $\frac{1}{2}^+$ state in ^{9}B by Barker [43] with the definition

$$\rho(E) = \frac{\frac{1}{2}\Gamma}{(E_r + \Delta - E)^2 + (\frac{1}{2}\Gamma)^2}, \tag{2.4}$$

where Γ is the width of the state, E_r is the resonance energy and Δ is a linear function of energy in the vicinity of the resonance. This analysis yielded an excitation energy of $1.8-1.9$ MeV for the state of interest, which was higher than the mirror state in ^{9}Be in contradiction to the other model predictions. This was mainly because the R-matrix analysis required an inverted Thomas-Ehrman shift on account of the mirror ^{9}Be state being above the ^{8}Be g.s + s-wave neutron threshold [43]. As shown in Fig. 2.3, there currently exists a large disagreement in the R-matrix predictions with the single-particle shell model calculations or microscopic cluster model. The situation with the experimental data indicates otherwise, as discussed in the next section.
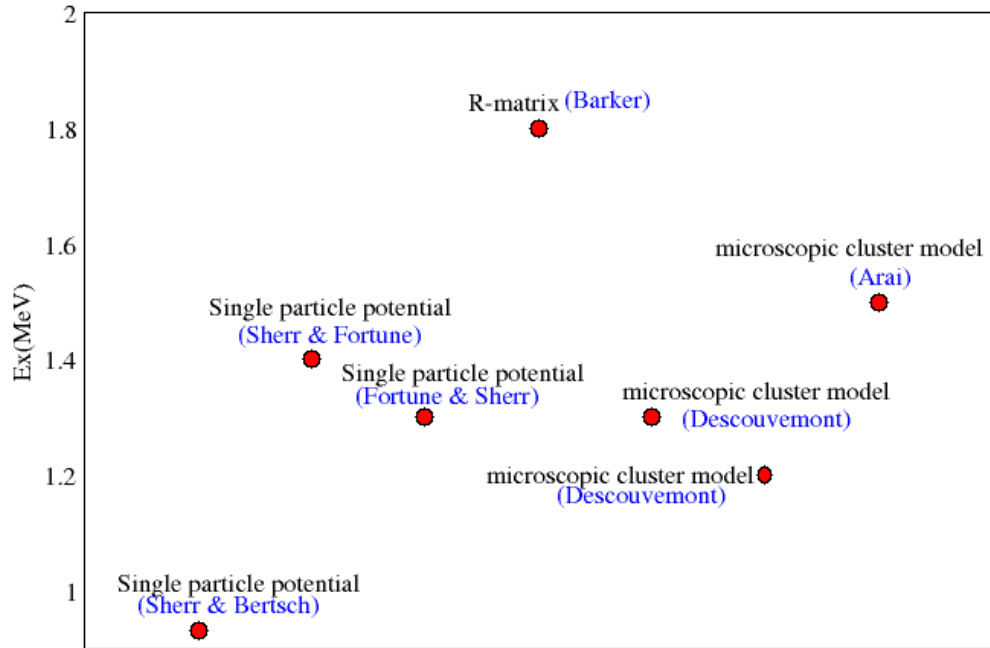
Figure 2.3: *Theoretical predictions for the first excited* $\frac{1}{2}^+$ *in* ^{9}B*, obtained by models discussed in the previous sections.*
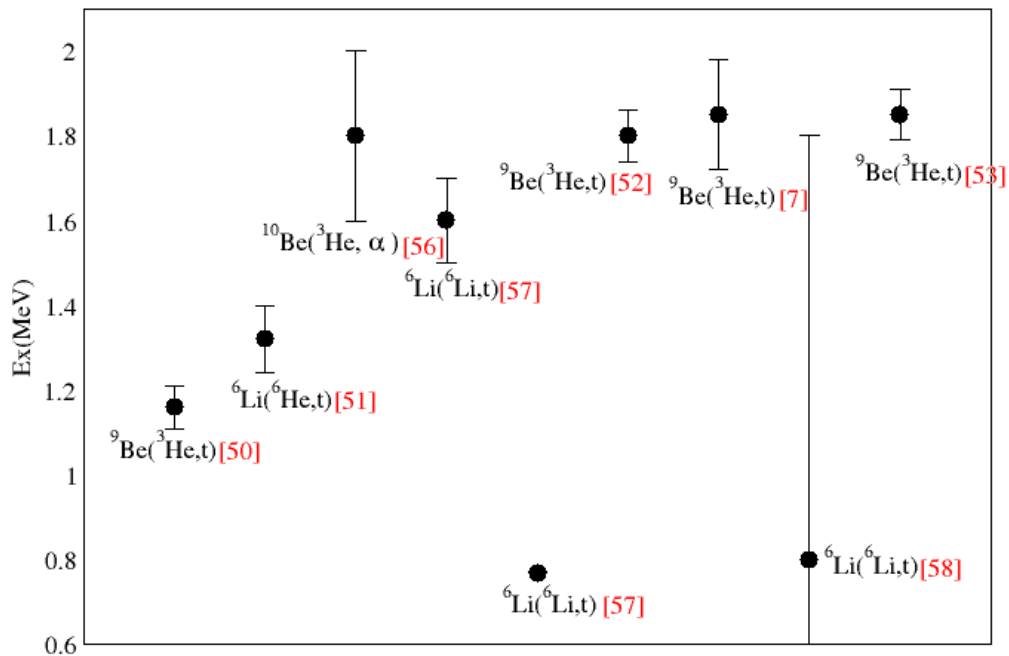
Figure 2.4: *Experimental determinations of the excitation for the first excited $\frac{1}{2}^+$ in ^{9}B.*

2.4 Past experimental investigations of the first $\frac{1}{2}^+$ state in ^{9}B

The first experiments to show the possible existence of the first excited $\frac{1}{2}^+$ state in ^{9}B were performed by Marion *et al* [44–46]. In their experiments, low-energy proton beams were bombarded on the ^{9}Be targets to study the ^{9}B$(p, n)^9$B reaction, using a pulsed-beam time-of-flight technique. They measured the excitation energy of the first $\frac{1}{2}^+$ state in ^{9}B to be 1.4 MeV

with a width of about 1 MeV. In 1960 Saji $et\ al$ [47] confirmed this observation, although the state appeared to be weakly populated in their experiment. In 1962, Symons and Treacy [48] observed the state using the $^{12}C(p, \alpha)^9B$ reaction and obtained its energy to be 1.7±0.20 MeV with $\Gamma \approx 1$ MeV. This work was followed by Teranishi and Furubayashi [49] who recognized that their fit to the near-threshold yield of neutrons from ^{9}Be$+p$ scattering data was improved by including a ^{9}B level at 1.7 MeV excitation. Following this work, Kroepfl and Browne [19] also detected a ^{9}B state at 1.5 MeV with a width of 0.7 MeV using ^{10}Be$(^3$He$, \alpha)^9$B reaction. In 1987, Kadija $et\ al$ [50] studied low lying states in ^{9}B using the $(^3$He$, t)$ reaction at the JULICH cyclotron facility and obtained the evidence for the state to be at 1.61±0.03 MeV with a width of 1.0 ± 0.2 MeV, following which Burlein $et\ al$ [51] investigated the ^{9}Be$(^6$Li,^{6} He$)^9$B reaction and obtained the broad peak at the excitation energy of 1.32 ± 0.08 MeV with a width of 0.86±0.26 keV for ^{9}B. More recently, research groups also used the ^{6}Li$(^6$Li$, t)^9$B reaction with state-of-the-art position-sensitive strip detectors, which yielded $E_x = 1.6 \pm 0.1$ MeV. This experiment was repeated at the Australian National University in 2003 with a more efficient setup. Quite surprisingly, this experiment determined the excitation energy of the $\frac{1}{2}^+$ state to be 0.73 ± 0.05 MeV with a width of ≈ 0.3 MeV, in large disagreement with previously measured values. This work was followed up by several other $(^3$He$, t)$ experiments [39,52,53], which contrastingly were in better agreement with the older measurements. Figs 2.3, 2.4 and Table 2.2 summarise the current situation. Clearly the R-matrix predictions agree with most of the experimental determinations and not the other theoretical models. On the experimental front, it is only one of the most precise determinations that agrees with cluster and single-particle potential model predictions while disagreeing with the rest. Clearly this situation demands further investigation and provides adequate motivation for this work.

Table 2.2: A summary of previous experimental determinations of first excited $\frac{1}{2}^{+}$ state in ^{9}B.

Author	E_x (MeV)	Γ (MeV)	Reaction	Year
Marion *et al* [44–46]	1.4	1	^{9}Be$(p,n)^9$B	1955-59
Saji *et al* [47]	1.4	1	^{9}Be$(p,n)^9$B	1960
Symons & Treacy [48]	1.7 ± 0.2	1	^{12}C$(p,\alpha)^9$B	1962
Barker & Treacy *et al* [42]	1.2	1	^{9}Be$(^3$He$,\alpha)^9$B	1962
Teranishi [49]	1.7	$-$	^{9}Be$(p,n)^9$B	1964
Slobodrian *et al* [54]	1.4	$-$	^{9}Be$(p,n)^9$B	1967
Kroepfl & Browne [19]	1.5	0.7	^{10}Be$(^3$He$,\alpha)^9$B	1968
Anderson *et al* [55]	1.4	0.0	^{9}Be$(p,n)^9$B	1969
Kadija *et al* [50]	1.16 ± 0.5	1.0 ± 0.2	^{9}Be$(^3$He$,t)^9$B	1987
Burlein *et al* [51]	1.32 ± 0.08	0.86 ± 0.26	^{9}Be$(^6$Li$,^6$He$)^9$B	1988
Arena *et al* [56]	1.8 ± 0.2	0.9 ± 0.3	^{9}Be$(^3$He$,\alpha)^9$B	1988
Tiede *et al* [57]	1.6 ± 0.1	0.77	^{6}Li$(^6$Li$,t)^9$B	1995
	0.73 ± 0.05	≈ 0.3	^{6}Li$(^6$Li$,t)^9$B	1995
Akimune *et al* [52]	$1.8\pm^{0.22}_{0.16}$	$0.600\pm^{300}_{270}$	^{9}Be$(^3$He$,t)^9$B	2001
Scholl *et al* [39]	1.85 ± 0.13	0.7 ± 0.27	^{9}Be$(^3$He$,t)^9$B	2011
Baldwin *et al* [58]	$0.8 - 1.0$	1.5	^{6}Li$(^6$Li$,t)^9$B	2012
Wheldon *at al* [53]	1.85 ± 0.06	0.650 ± 125	^{9}Be$(^3$He$,t)^9$B	2015

CHAPTER 3

EXPERIMENTAL APPARATUS AND TECHNIQUES

3.1 Experimental approach

As mentioned previously, our experimental approach was to produce the first excited $\frac{1}{2}^+$ state in ^{9}B using ^{9}B(^{3}He, t)^{9}B* reaction. Because the ^{9}B states are particle unstable, it mainly breaks up into a proton and ^{8}Be, which in turn breaks into two alpha particles, as shown schematically in Fig. 3.1. Part of the experiment was used to determine the energy of the second $T = 3/2$ state in ^{9}B in order to test the IMME for the excited $T = 3/2$ quartet for $A = 9$. In this chapter I describe the apparatus used for these measurements.
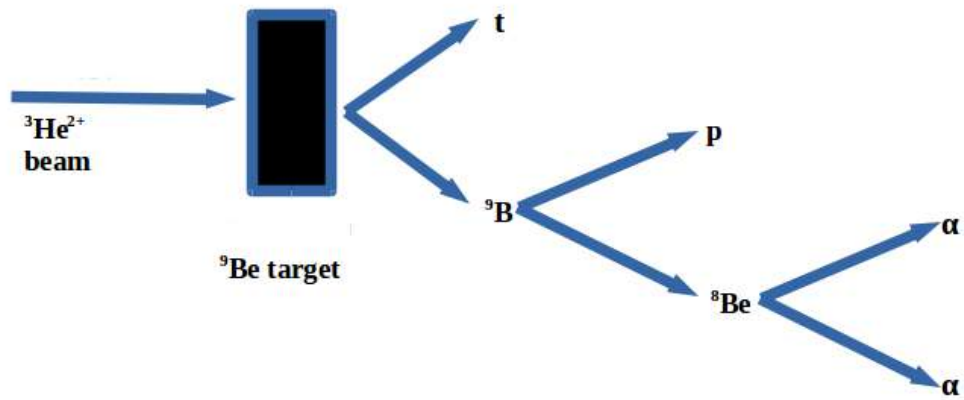
Figure 3.1: *Sequence of break-up particles emitted from excited states in* ^{9}B*, populated using the* ^{9}Be$(^3$He$, t)^9$B *reaction. Figure adapted from Ref. [32].*

3.2 The iThemba LABS cyclotron facility

All the measurements described in this thesis were conducted at iThemba LABS, a multi-disciplinary facility situated in Somerset West, near Cape Town. This accelerator facility provides high-energy beams of different ions, which can be extracted and used in a wide range of applications, such as radioactive isotope production, proton and neutron therapy, radiation biophysics and basic research. The basic research conducted at iThemba LABS includes an intensive program for fundamental nuclear physics and material sciences. The most important feature of this facility is the Separated Sector Cyclotron (SSC) accelerator shown in Fig. 3.2. The light or heavy ions are pre-accelerated by one of the two solid pole injector cyclotrons (SPC1 and SPC2) until they gain energy sufficient enough to be transported to the SSC. From the SSC the beams can be steered along different beam lines and transported to different experimental facilities. For our experiment the beam was transported to the K600 magnetic spectrometer vault through the X, P and S beam lines.
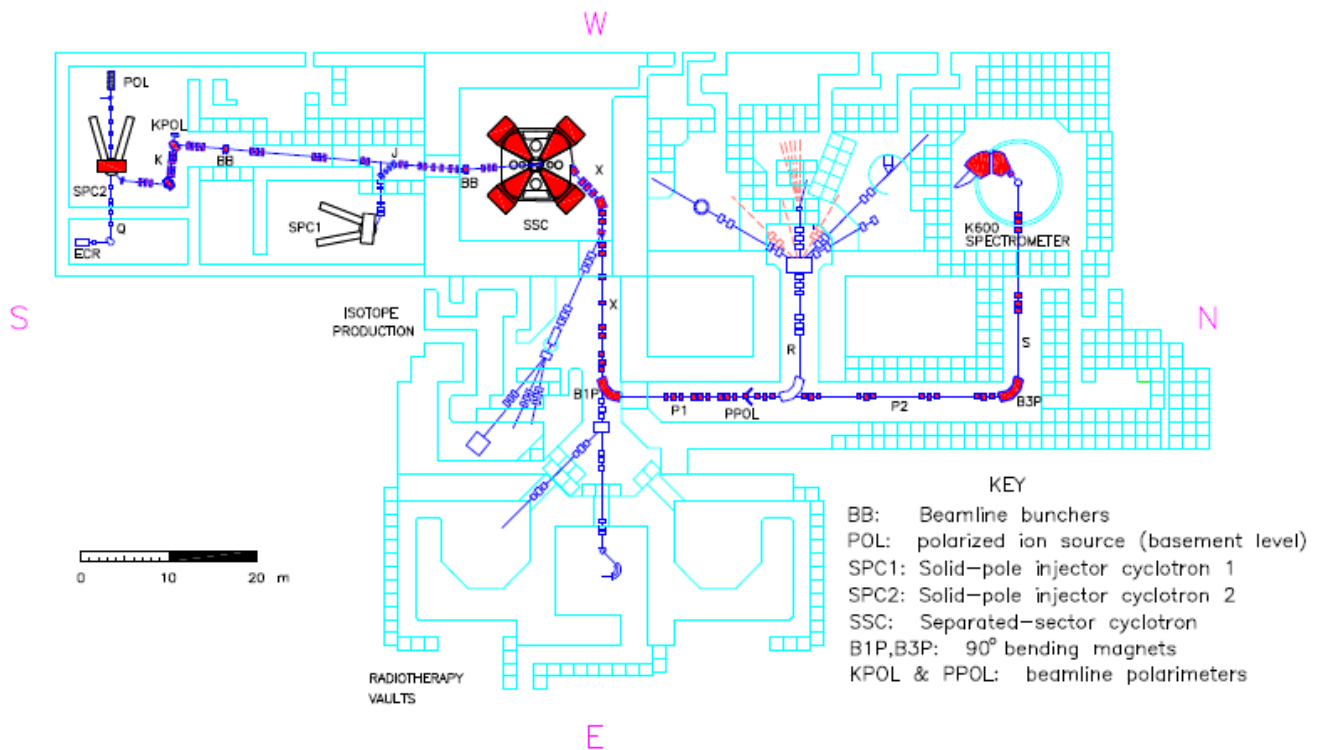
Figure 3.2: *Layout of the Separated Sector Cyclotron facility of iThemba LABS. Figure taken from [59].*

3.3 Scattering chamber

The scattering chamber used for this experiment was newly developed for measurements to be performed at $0°$ to the beam direction. It is made of stainless steel, and located at the turning axis of the spectrometer, connecting the end of the beamline to the entrance of the magnetic spectrometer. The target ladder has the provision to mount six targets, as well as a turntable on which an internal beamstop or detectors can be mounted, depending on the experimental setup of interest. A picture of the chamber is shown in Fig. 3.3.
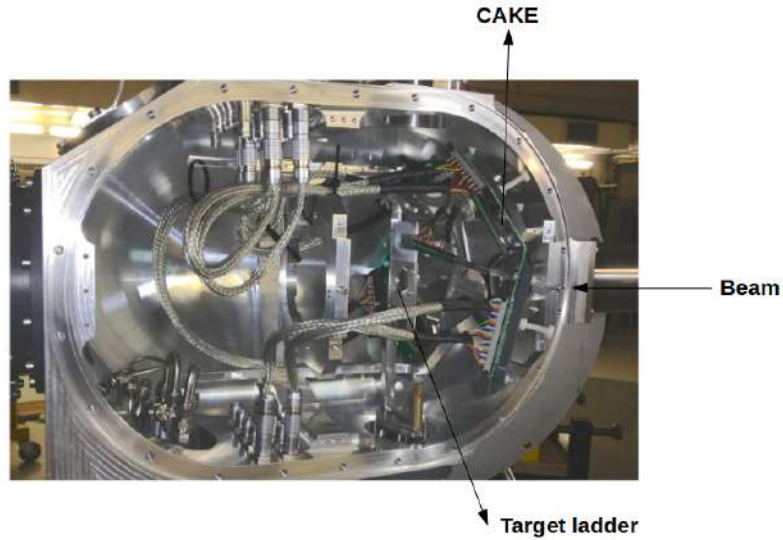
Figure 3.3: *The new scattering chamber setup with the CAKE mounted at backward angles. Figure taken from [59].*

For this experiments we also mounted an ancillary detector system called CAKE (the Coincidence Array for K600 Experiments) [60] to detect unbound protons from excited states in ^{9}B. However, these data were not used for the final analysis, as the highly unbound nature of the states in ^{9}B distort the proton spectra as well.

3.4   Target preparation

Three targets were used in this experiment. These are listed as

- ^{9}Be foil of thickness of 10.21 ± 0.41 μm

- ^{9}Be foils of thickness of 4.41 ± 0.20 μm

- ^{26}Mg foil of thickness of 3.86 ± 0.10 μm for energy calibration

A picture of these targets mounted on the K600 target ladder is shown in Fig. 3.4

Figure 3.4: ^{9}Be *and* ^{26}Mg *targets mounted on the K600 target ladder.*

All of these targets were prepared using the mechanical rolling method, an economical and simple technique that has been used to produce the self-supporting targets for many years. However it is challenging to produce reasonably thin self-supporting ^{9}Be targets. We used a mechanical rolling mill for which a double packing was also used. These are showed in Fig. 3.5. We produced one ^{9}Be target that was $\approx 4 \ \mu m$ thick. A much thicker ^{9}Be target was purchased from Goodfellow. Regrettably the company shipped an $\sim 2 \ mg/cm^2$ thick target instead of the requested 200 mg/cm^2 thickness. Nevertheless, this thick target was also used in our experiment.

Figure 3.5: *The mechanical rolling mill is shown on the left hand side and the stainless-steel pack on the right hand side.*

The ^{26}Mg target material was bought from Oak Ridge National Laboratory and isotopically enriched to 99.4%.

3.5 K600 Magnetic spectrometer

The high resolution K600 magnetic spectrometer [61] at iThemba LABS was used to detect the reaction tritons for our measurements. The spectrometer is shown in Fig. 3.6. It consists of five electromagnets, namely a quadrupole, two dipoles, and two trim coils (K and H). The quadrupole magnet Q is used to focus the scattered particles vertically immediately after collimation in the focal plane. The two dipole magnets D1 and D2 are the important bending magnets of the spectrometer. They allow the momentum dispersion to be adjusted by varying the two dipole magnet settings. Additionally, the two trim coils, positioned inside the dipoles are used for the final focusing at the focal plane. The K-coil, a pole-face current winding which introduces both a quadrupole and dipole component, provides the first order kinematic variation of the momentum ejectiles with angle $(x|\theta)$. The H-coil, another pole-face that introduces both a dipole and sextupole component, provides the corrections for

$(x|\theta^2)$ abberations. A crucial aspect of the device is its ability to run experiments in a $0°$ mode [61]. A collimator placed inside the scattering chamber imposes a $\pm 2°$ restriction (centred at $0°$) for scattered particles to be accepted to the spectrometer. The focal plane position-sensitive detectors are situated behind the second dipole. The focal plane detectors allow measurements to be taken in the low, medium or high dispersion modes. I discuss these briefly below.
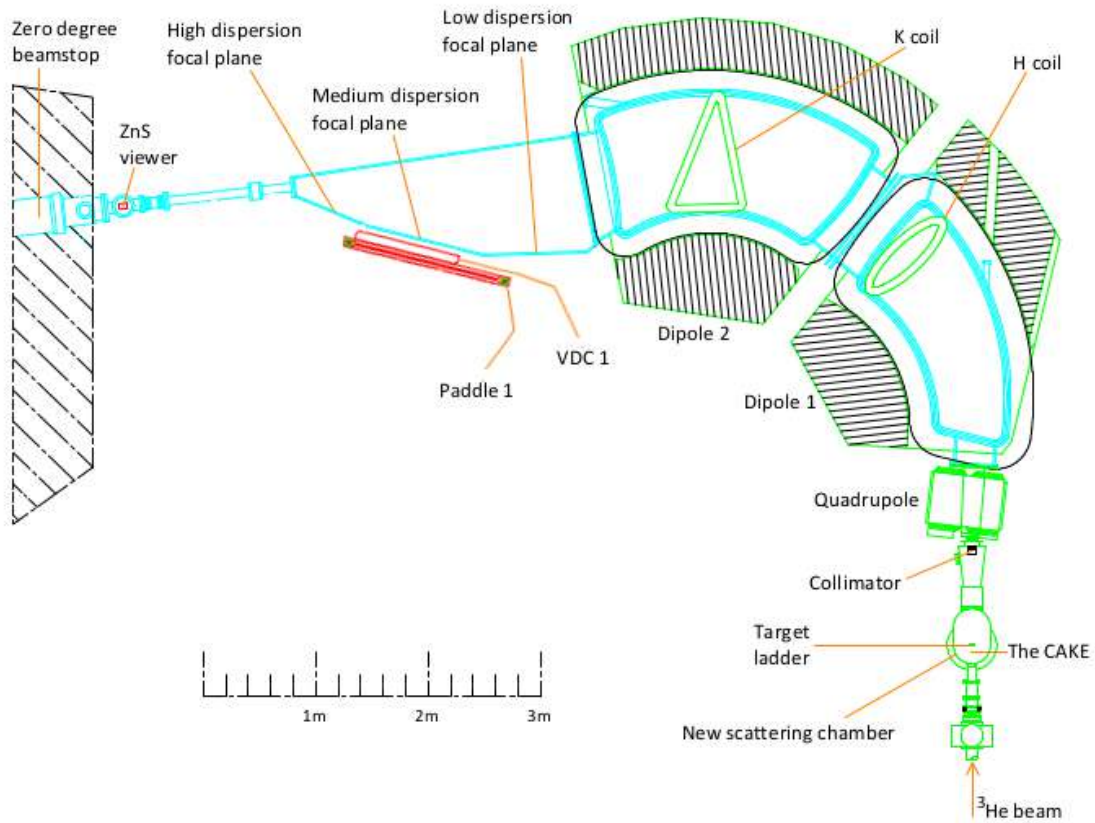
Figure 3.6: *Top view of the K600 magnetic spectrometer configured in the $0°$ mode.*

3.6 The focal plane detector system

The focal plane detector system of the K600 magnetic spectrometer consists of two important components, the vertical drift chambers (VDCs) and the plastic scintillators (also known as paddles). In this experiment only one VDC/paddle combination was used due to the low energy of the outgoing tritons[1]. The main aim of the VDCs is to determine the position and angle at which specific charged particles cross the focal plane. The plastic scintillators situated behind the drift chambers are used for trigger signals for the events and for particle identification. Both these detector systems are described below.

3.6.1 Vertical drift chambers (VDCs)

The VDCs are gaseous ionization detectors whose main purpose is to track scattered particles and analyse the excitation energies of the recoil nuclei. In this experiment one VDC was used in a medium dispersion focal plane configuration. The VDC consists of two wire planes: an X and a U wire plane. The X wire plane is perpendicular to the scattering plane, while in the U wire plane the wires are angled at 50° with respect to the scattering plane. The X wire plane provides horizontal information of the scattered particle while a U wire plane provides both horizontal and vertical information. Each VDC consists of three high-voltage planes that separate the detector into an X and a U wire chamber. The high-voltage (HV) planes are made from streched aluminium foil. Mylar windows are used to isolate the VDC wire chambers from atmosphere. Fig. 3.7 shows a cross section of the VDC used for this experiment.

---

[1]Other K600 spectrometer experiments use two VDC's and plastic scintillators for improved resolution.
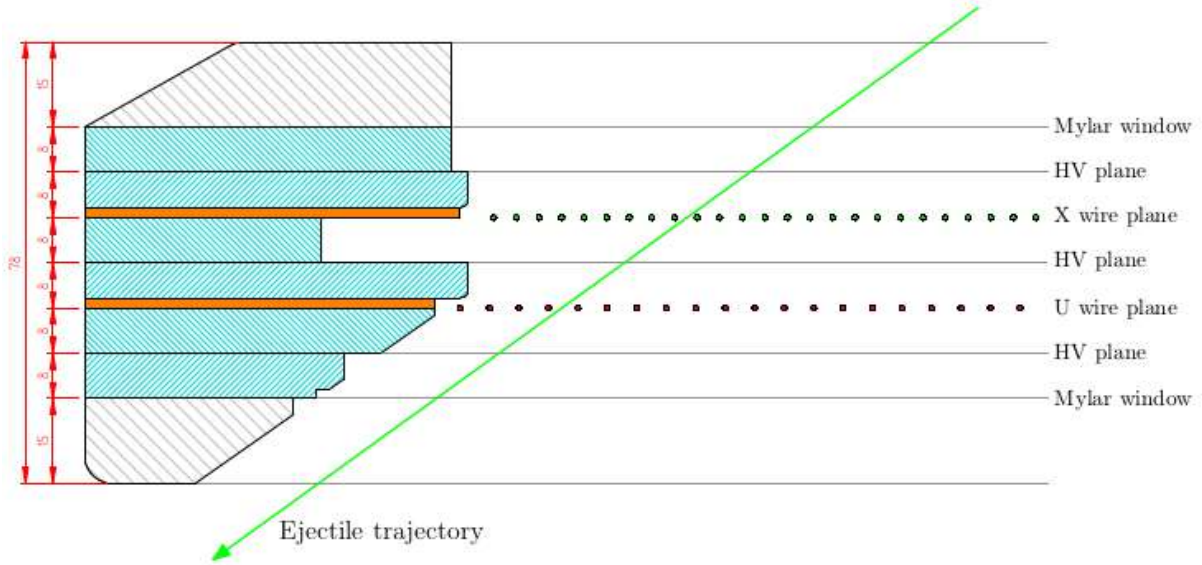
Figure 3.7:   *Cross-sectional top view of a VDC [59].*
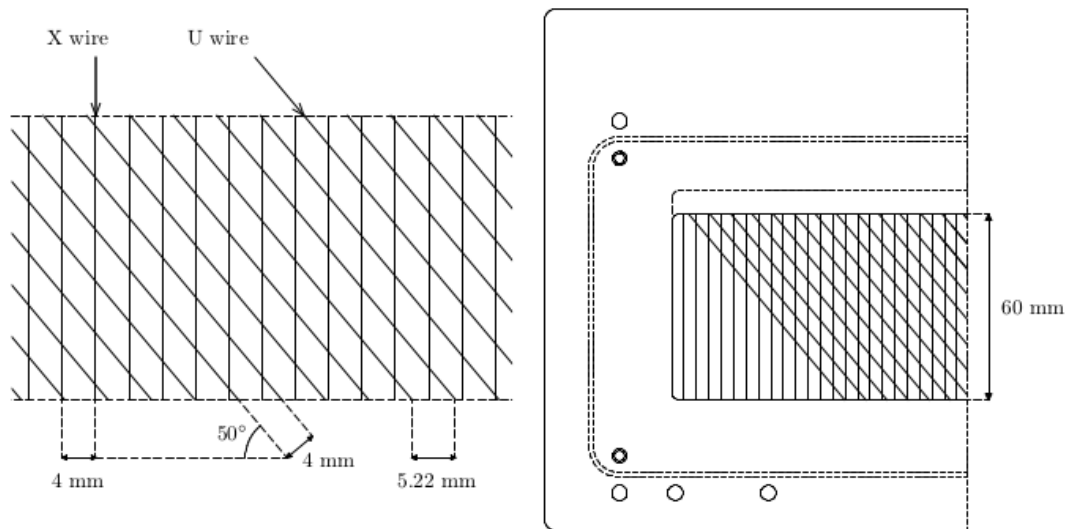
Figure 3.8:   *This figure shows the side view of the VDC wire planes. Taken from [59].*

The X and U wire planes are sheltered within the wire chambers of the VDCs. Each X wire plane consists of 198 signal wires and 201 guard wires while each U wire plane consists of 143 signal and 146 guard wires. The X wires are positioned vertically while the U wires are

42

angled 50° with respect to the horizontal plane. All signal wires are positioned such that the normal/minimum distance between neighbouring signal wires of a particular wire plane is 4 mm. A side view of the wire planes is shown in Fig. 3.8.

3.6.2 Plastic scintillator (paddle)

As mentioned before, the plastic scintillator paddles are positioned behind the drift chambers and used to generate the event trigger signals and for particle identification. They are made of BC-408 plastic scintillation material, manufactured by Saint Gobain. The choice of BC-408, suitable for measuring charged particles, is due to their very short response times. The paddles have a surface area of 48"× 4"and their thickness ranges from $\frac{1}{8}$"to about $\frac{1}{2}$". We used the latter for this measurement.

Figure 3.9:   *The K600 scintillator paddles. The material is insulated from external light sources by having the paddles wrapped in Mylar. The image on the right shows the light guides which couple the scintillators to their photomultiplier tubes [59].*

The choice of thickness depends on the scattered particle of interest and on its energy. In other cases, if the charged particles have sufficient energy to pass through the VDCs and the first

paddle ΔE, a second paddle can be used as an E detector. In this case the paddle coincidences would be used for triggering and the additional particle identification information can be obtained through $\Delta E - E$ spectra.

CHAPTER 4

DATA ANALYSIS

In this chapter I discuss the analysis of the experimental data obtained from our $^9\text{Be}(^3\text{He},t)$ measurement. During the experiment, raw data were collected by the MIDAS [62] data acquisition (DAQ) system in the form of event files. An online analysis code that was previously written explicitly to analyze K600 spectrometer data was further modified to carry out an offline analysis on the data of an event-by-event basis. Different subroutines in the code were used to convert the data into ROOT [63] files that were subsequently used for the offline analysis.

4.1 Particle Identification (PID)

The first step in the analysis procedure was to identify the particles detected at the focal plane from $^9\text{Be}+^3\text{He}$ reactions. In order to select only the tritons from $^9\text{Be}(^3\text{He},t)^9\text{B}$ reactions, a particle identification gate must be applied on the data. Since, the energy deposited on the paddles is observed as the integrated charge from the photomultiplier tubes (PMTs), in conjuction with the time of flight (TOF) of the ejectiles, this PMT signal can be used to define the particle identification (PID) gates. The TOF is calculated with respect to a common stop signal provided by the RF from SSC. By plotting the energy deposited in

the scintillator paddle against the TOF, various PID loci become visible. As mentioned previously, we obtained the data using two spectrometer field settings to study both the low and high excitation energy regions of ^{9}B. The PID spectra for both these field settings are shown in Figs. 4.1 and 4.2. In the high excitation region the charged particles transported to the focal plane were uniquely identified by gating on the triton and deuteron loci enclosed by the rectangular PID gates shown in Fig. 4.1. In the low-lying region the same procedure was used to gate on the tritons as shown in Fig. 4.2. Those PID gates were used to generate the final focal plane position spectra.
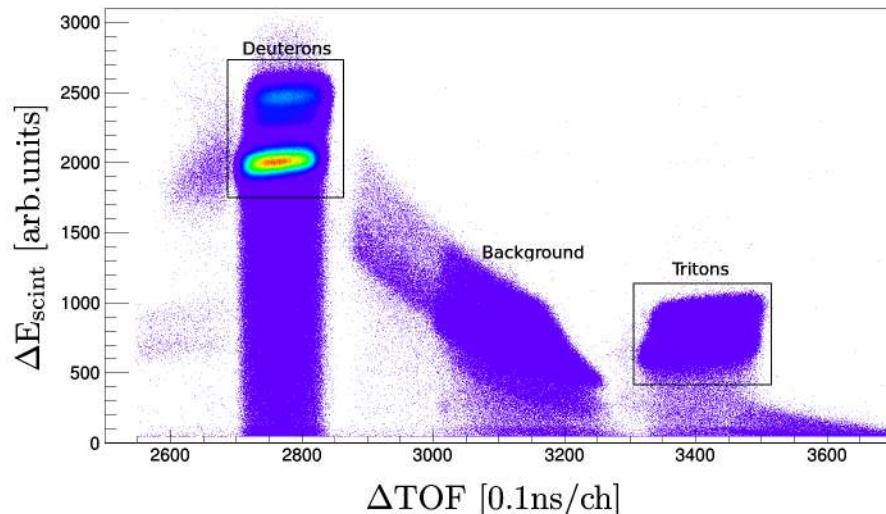
Figure 4.1: *Two-dimensional PID plots for the high excitation region with a ^{9}Be target. We observe that two types of charged particles were detected at the focal plane, corresponding to ^{9}Be(^{3}He, d)^{10}B and ^{9}Be(^{3}He, t)^{9}B reactions.*

To further cross check our particle identification, we performed some elementary calculations for the expected TOF. These calculations were done for the charged particles expected at the focal plane, based on their rigidity. The TOF calculation was performed by using the simple relationship

$$TOF = \frac{d}{v}, \tag{4.1}$$

46
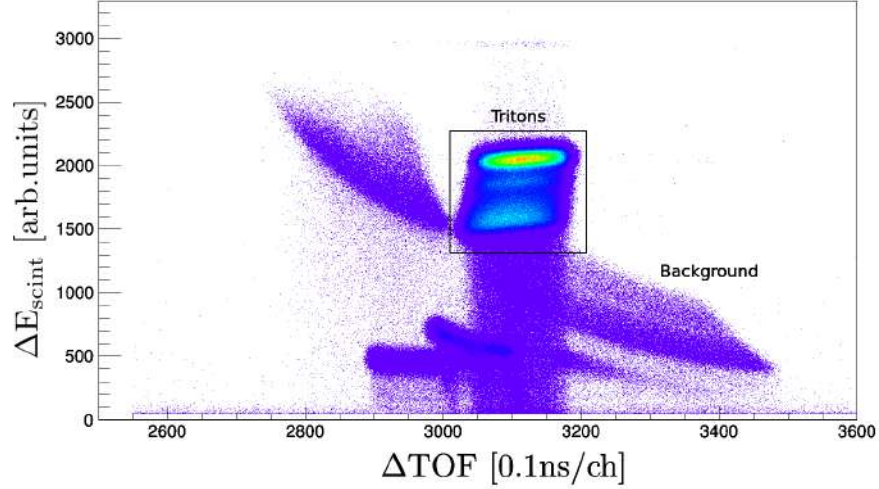
Figure 4.2: *The two-dimensional PID plot for the low-lying excitation region with the* ^{9}Be *target. Only one type of charged particles (tritons) were detected at the focal plane, highlighted by the rectangular box.*

where d is the flight path of the ejectile particle within the K600 spectrometer (which is on average 8.14 m) and v is the velocity of the particle. The velocity can be calculated relativistically using,

$$v = c\sqrt{1 - \left(\frac{M}{E_{tot}}\right)^2} \tag{4.2}$$

where c is the speed of light, M is the rest mass and E_{tot} is the total energy of the particle.

4.2   Background investigation with an empty frame

As mentioned before, the data for this experiment were obtained with the K600 magnetic spectrometer running in a zero-degree mode. Therefore an accurate understanding of the beam induced background was necessary. This background is prominent in 0° measurements due to the location of the beam stop very close to the sensitive region of the spectrometer. An additional source of background is from beam halo scattering off the target frame.
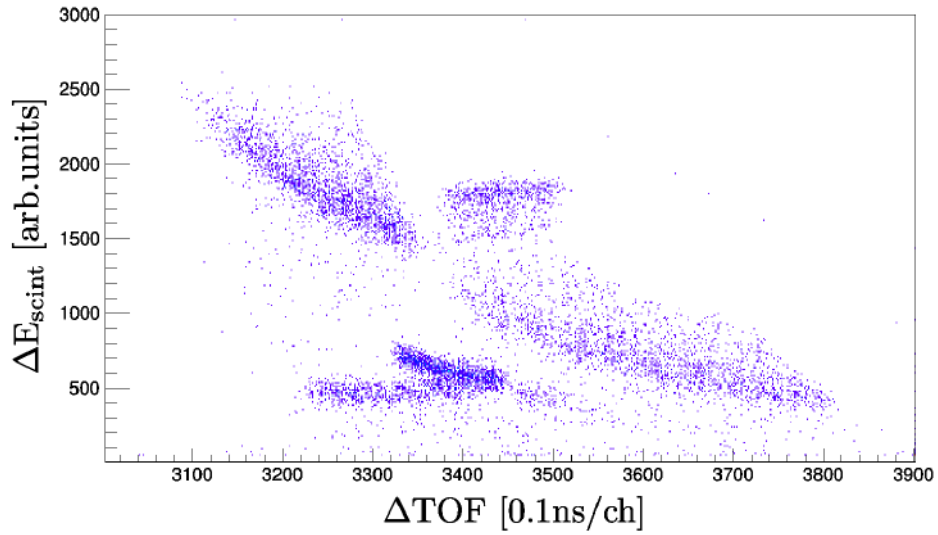
Figure 4.3: *Two-dimensional PID plots for the low-lying excitation field settings with an empty frame, showing the background originating from the beam halo.*
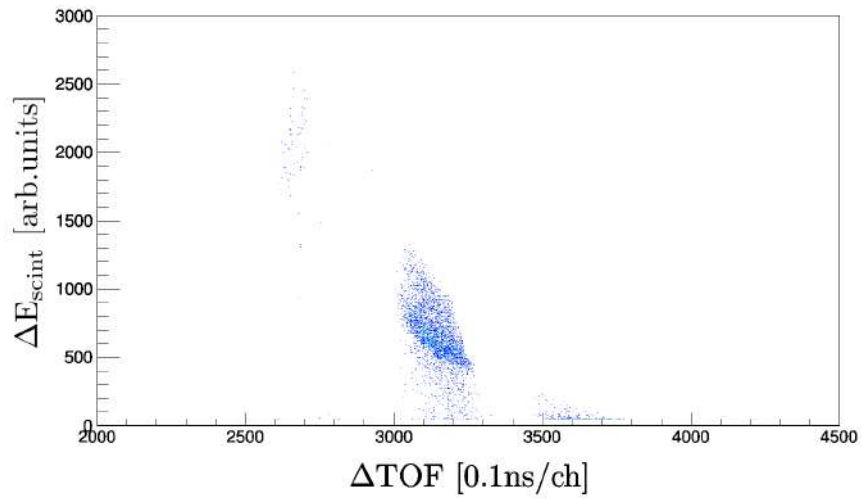
Figure 4.4: *Two-dimensional PID plot for the high excitation region with an empty frame, showing the background originating from the beam halo.*

To better quantify this background, we took additional data with an empty target frame. Figs. 4.2 and 4.3 show a comparison of the PID spectra both with an empty frame and a ^{9}Be target for the lower excitation field settings, while Figs. 4.1 and 4.4 show a similar comparison for the high excitation field settings.

4.3 Relativistic kinematics

I now briefly discuss the kinematics of two-body nuclear reactions. Our reaction has the form

$$a + B \rightarrow C + d \tag{4.3}$$
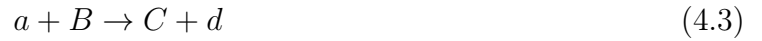
where a is the beam, B is the target, C is the recoil nucleus which breaks up into two lighter fragments $(C \rightarrow e + f)$ and d is the light ejectile. In this work, the kinematics for the reaction was calculated using relativistic formulae.
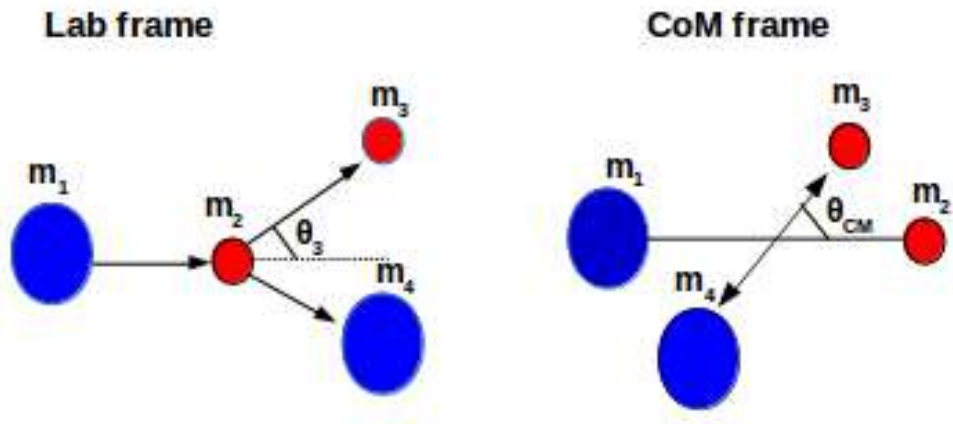
Figure 4.5: *Representation of a two-body nuclear reaction in both laboratory and centre-of-mass frames.*

Fig. 4.5 shows the difference between the laboratory and centre-of-mass frames for the above reaction, assuming the masses of a, B, C and d are m_1, m_2, m_3, and m_4 respectively. Setting $c = 1$, the Q-value for the two-body reaction is defined by

$$Q = m_1 + m_2 - (m_3 + m_4). \tag{4.4}$$

If, for convenience, we set $c = 1$, the total energy of the laboratory frame takes the form

$$E_T = E_1 + E_2 = E_3 + E_4. \tag{4.5}$$

In the centre-of-mass frame, the total momentum is zero, this implies that the total energy is given by

$$E_T' = (m_1 + m_2^2 + 2m_2E_1)^{1/2}. \tag{4.6}$$

Then, after a lot of algebra, the laboratory scattering energy light ejectile can be simply written as [64]

$$
\begin{aligned}
E_3 = & \frac{1}{E_T^2 - p_1^2 cos^2\theta_3}\{E_T(m_2E_1 + \frac{m_1^2 + m_2^2 + m_3^2 - m_4^2}{2}) \\
& \pm p_1 cos\theta_3[(m_2E_1 + m_1^2 + m_2^2 - m_3^2 - m_4^2)^2 - m_3^2 m_4^2 \\
& - P_1^2 m_3^2 sin^2\theta_3]\}.
\end{aligned}
\tag{4.7}
$$

Eq. 4.7 is expressed in terms of masses, energies E_T and E_T' and the laboratory scatttering angle θ_3. The $\pm$ sign in Eqn. 4.7 shows that there may be two solutions for E_3. The quantity that decides the $\pm$ sign is given by

$$\alpha = \frac{P_1}{E_T}\left(\frac{1 + \frac{m_3^2 - m_4^2}{E_T'^2}}{\{[1 - (\frac{m_3 + m_4}{E_T'})^2][1 - (\frac{m_3 + m_4}{E_T'})^2]\}^{1/2}}\right). \tag{4.8}$$

50

If $\alpha > 1$, both solutions in Eqn. 4.7 are valid and if $\alpha < 1$ only one solution is physically realistic, since the value inside the square root cannot be negative. The energy of the recoiling target-like nucleus in the laboratory frame is

$$E_4 = E_T - E_3. \tag{4.9}$$

The above algebra was used to write a relativistic kinematics program, whose purpose was to calculate the excitation energies for different final-state nuclei from various nuclear reactions.

4.4   Target thickness determination

Prior to the actual experiment, we determined the ^{9}Be and ^{26}Mg target thicknesses using a vacuum chamber in the iThemba LABS target laboratory [65], together with a 500 μm thick Si surface barrier detector from ORTEC.
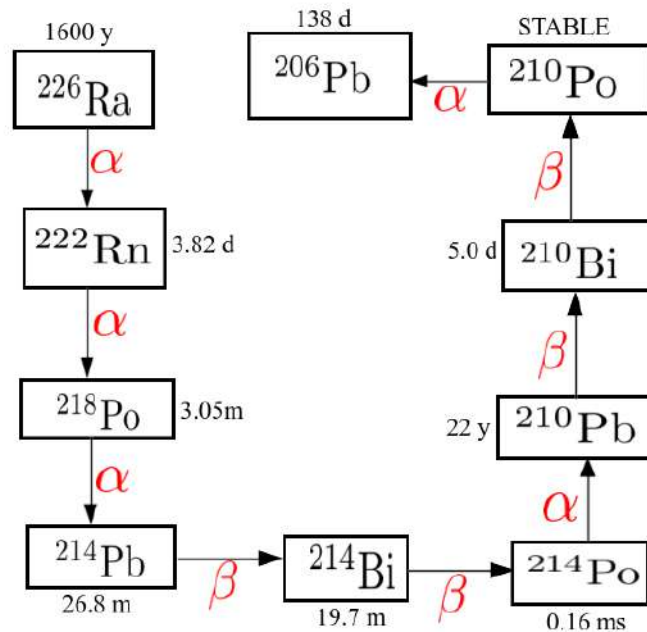
Figure 4.6:   *The decay chain of* ^{226}Ra α *source.*

The silicon detector was calibrated using a ^{226}Ra α source that was positioned on a target ladder and placed inside a high-vacuum scattering chamber. The decay chain of ^{226}Ra is shown in Fig. 4.6. Clearly, one would expect at least four α peaks in the Si detector from the decay of this nucleus. These α peaks would have energies ranging from 4.8 to 7.7 MeV and are shown in Fig. 4.7 and 4.8.
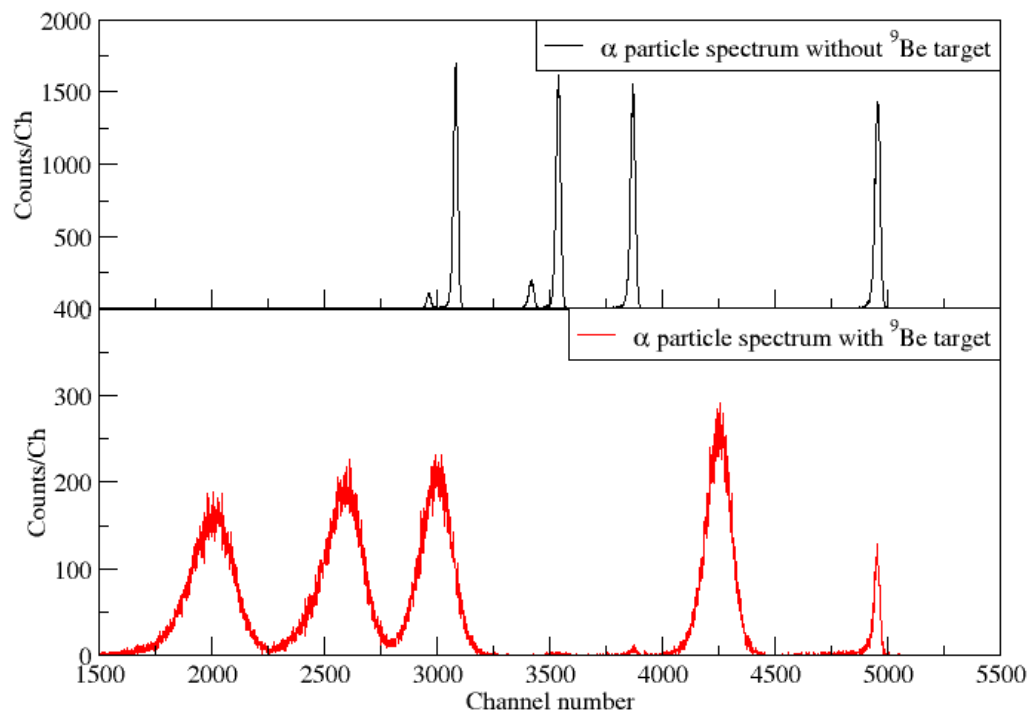
Figure 4.7: α spectrum from the decay of ^{226}Ra registered with the Si detector with and without a ^{9}Be target placed in between the source and the detector.

52
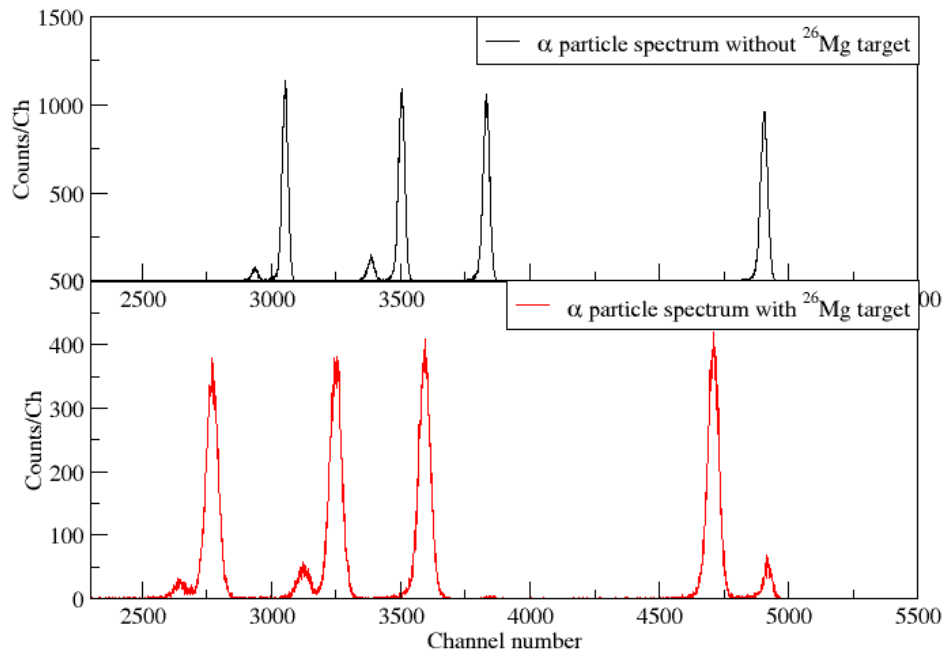
Figure 4.8: ^{226}Ra α spectra obtained with and without the ^{26}Mg target foil.

The top spectra in these figures were obtained with no targets placed between the source and the detector. The bottom spectra were obtained after placing the respective target foils between the source and the detector. The peaks in the latter appear at lower energies and are considerably wider than the peaks in the former. This is due to energy loss and straggling of the α particles through the target foils. As the α's emitted from the ^{226}Ra source have well known energies and the energy loss of charged particles within matter is directly proportional to the amount of material (thickness) within the transversed distance. Therefore, the energy shift in the α-peaks shown in Fig. 4.7 and 4.8 provide a direct measure of the thickness of the target foils. I briefly describe the procedure to extract target thicknesses below. The first step in the target thickness determination analysis was to fit the measured α peaks. The peaks were then fitted using a Levenberg-Marquardt χ^2 minimization routine using a
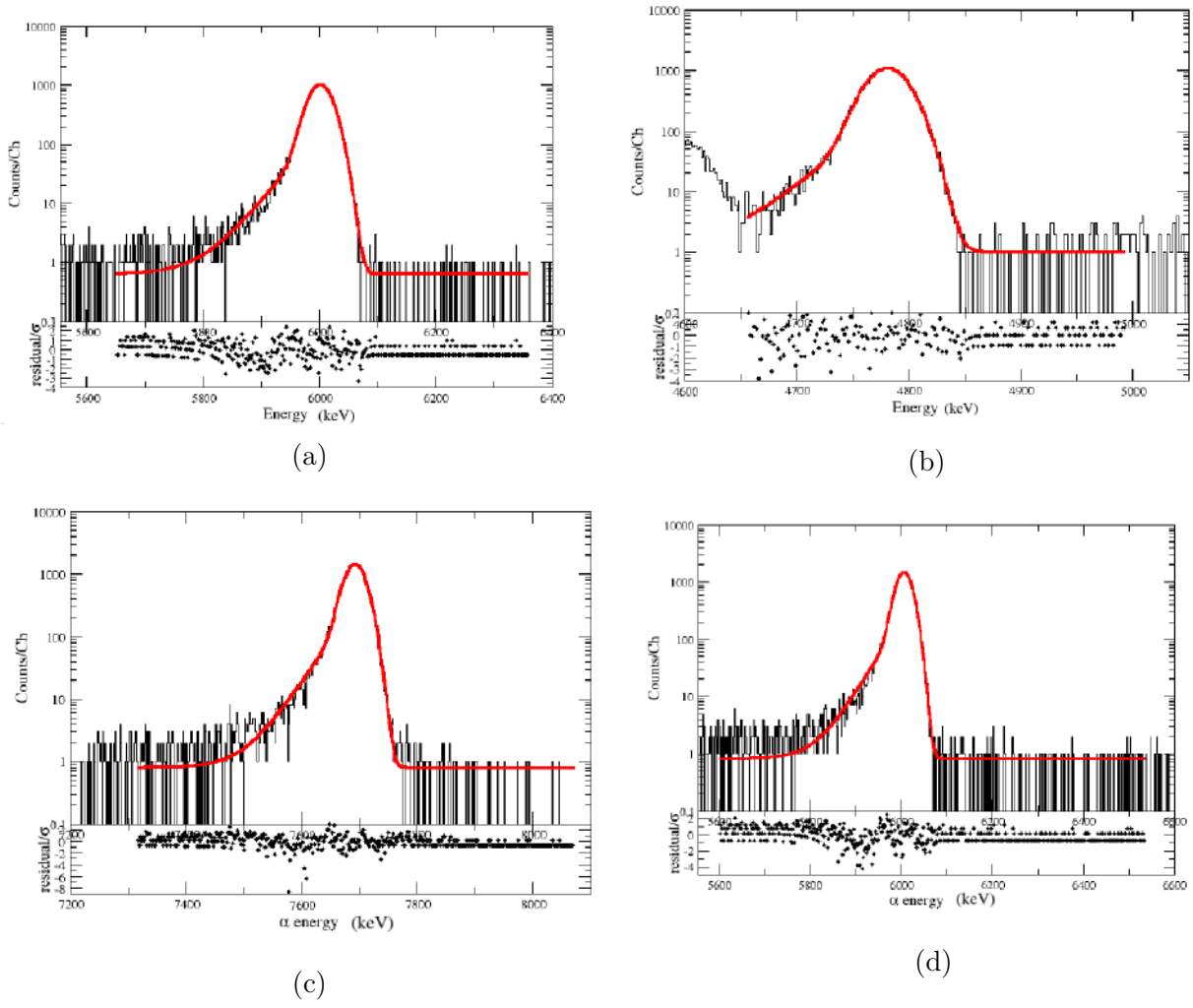
Figure 4.9: Sample fits to different peaks from the α-source with no target.
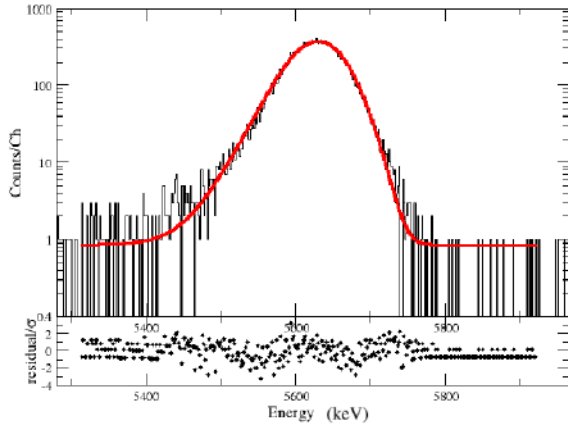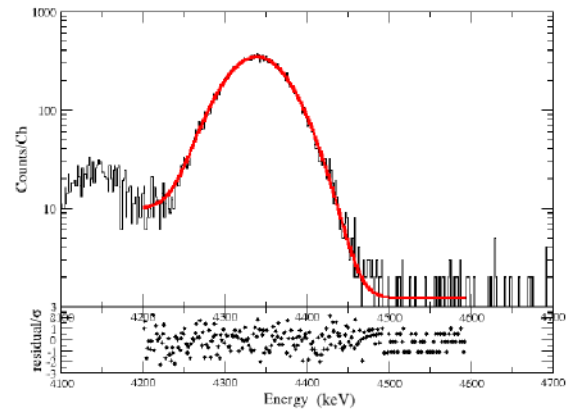
Figure 4.10: Sample fits to different peaks from the α-source with ^{26}Mg target.
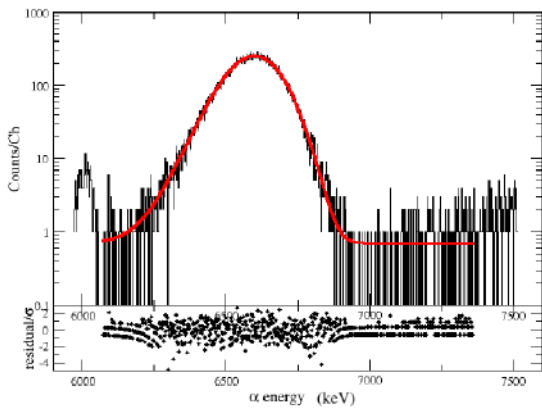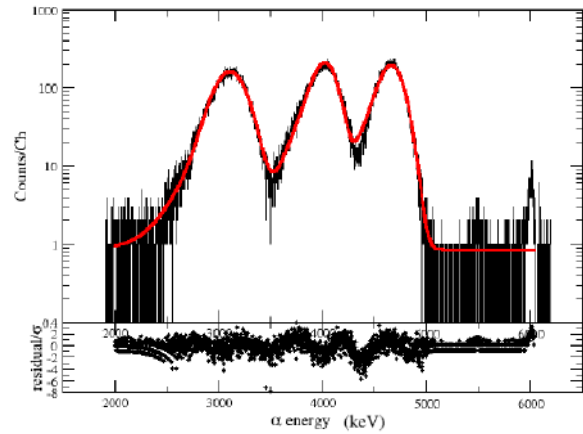
Figure 4.11: Sample fits to different peaks from the α-source with the ^{9}Be target.

lineshape function that was the convolution of a Gaussian with low energy exponential tails on a flat background, that was an additional free parameter. Some representative peaks and their corresponding fits are shown in Figs. 4.9 and 4.10, 4.11 and 4.11. The extracted α peak centroids from these fits were then used to perform a linear energy calibration

$$E_X(i) = a + bX(i) \tag{4.10}$$

where $X(i)$ are the peak centroids. The a and b calibration coefficients from above were used to determine the shifted peak energies from the α spectra obtained with the targets in place. The shift in the measured α- energy for each peak was used to independently extract the target thickness using an iterative algorithm that is described below. The final target thickness for each target was eventually determined by taking a weighted mean of the thickness values obtained from each α peak.

The first step in the iteration code was to input the values for the initial stopping powers $(\frac{dE}{dX})$ for the unattenuated α energies, which were calculated using the SRIM [66] software. We assumed 10% relative uncertainties in the stopping powers obtained from SRIM [66]. These values were then fit to a polynomial function of order 4 to obtain the (dE/dX) values for the unattenuated α energies shown in Figs. 4.12 and 4.13. Next the iteration procedure followed the flow chart shown in Fig. 4.14 over infinitesimal slices of target material ($\Delta X = 5 \times 10^{-6} \ \mu m$) over which (dE/dX) value was assumed to be constant, until the reduced α energies matched the attenuated values shown in Figs. 4.7 and 4.8.
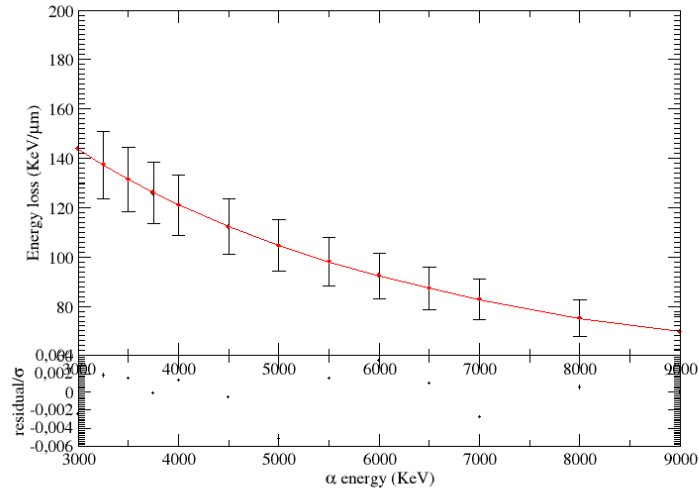
Figure 4.12: *Fit to the α stopping powers for ^{26}Mg target. The interpolation was obtained from a polynomial fit.*
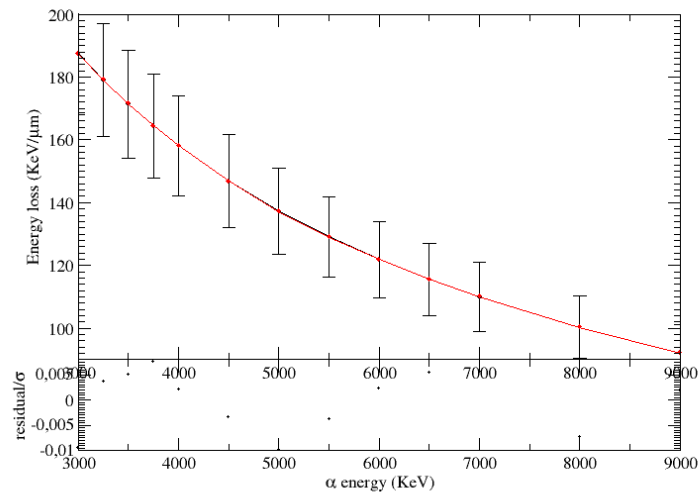
Figure 4.13: *Fit to the α energies stopping powers for ^{9}Be target. The interpolation was obtained from a polynomial fit.*
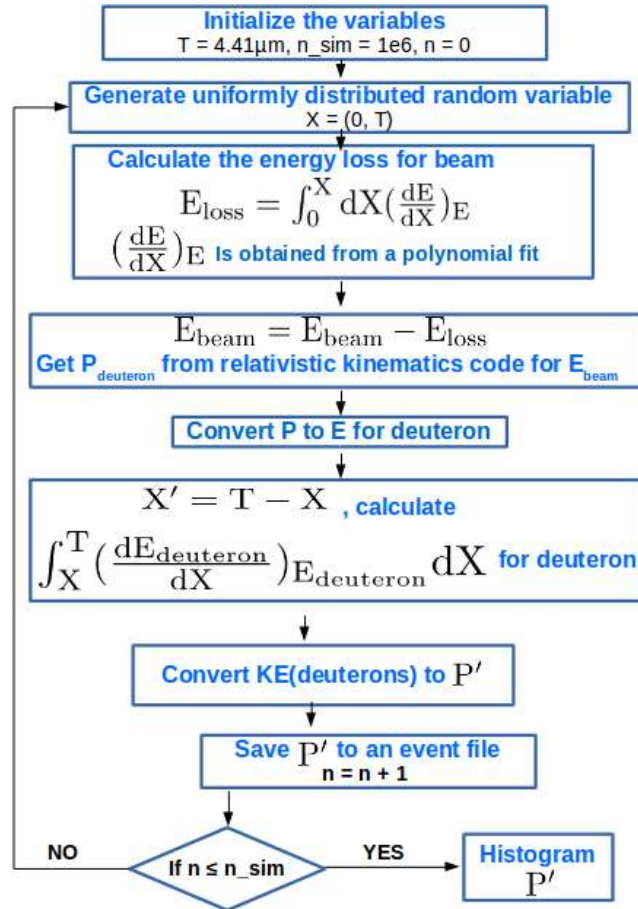
Figure 4.14: *Flow chart of the target thickness calculation code. E_α are any of the unattenuated α energies (with no target). E'_α are the reduced α energies, measured after passing through the targets.*

The final target thickness results for both the targets are shown in Table 4.1. The dominant contribution to the uncertainties in these results arises from the fits to the α peaks shown in Figs. 4.9 to 4.11.

Table 4.1: Extracted ^{9}B and ^{26}Mg target thicknesses.

Target	Thickness (μm)
^{9}Be	4.41 ± 0.20
^{26}Mg	3.86 ± 0.3

4.5 Energy resolution improvement

The energy resolution obtained at the focal plane can be improved further in the offline data analysis by using a lineshape correction technique [67]. This technique is used to correct the data for abberations that are not fully corrected with the K and H coils. Since the focal plane position depends on the scattering angle of the ejectile, this dependency can be reduced by using a linear correction. The linear correction was achieved by plotting the TOF of the tritons against focal plane position spectrum, shown in Fig. 4.15. It is easy to
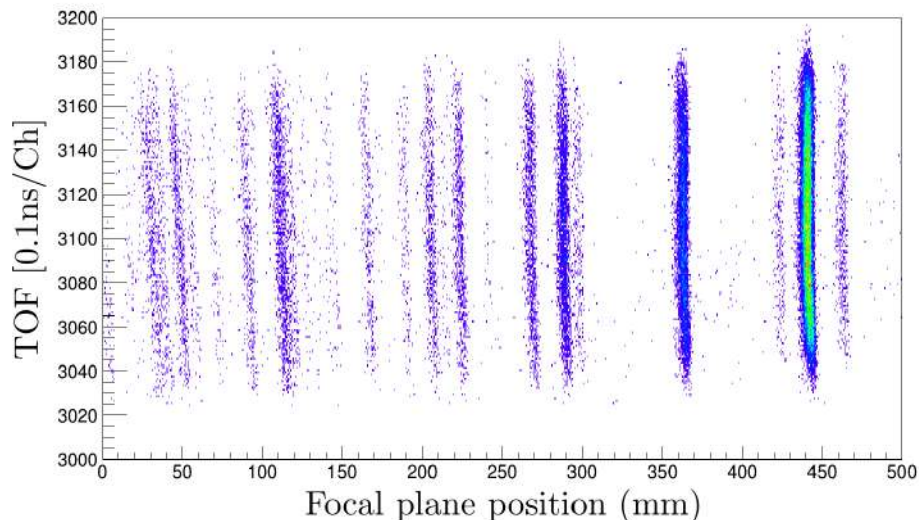
Figure 4.15: *TOF of tritons versus the focal plane position before the lineshape correction.*

observe that the locus of points shown in Figs. 4.15 and 4.16 have a curved shape which results in poor energy resolution. In order to further improve the resolution the linear fit correction was performed, whose results are shown in Fig. 4.17. Although this is a standard procedure followed in K600 experiments (see [61]), we do not observe a noticeable change in the resolution of the focal plane spectrum due to this correction. This is shown in Figs. 4.18 and 4.19
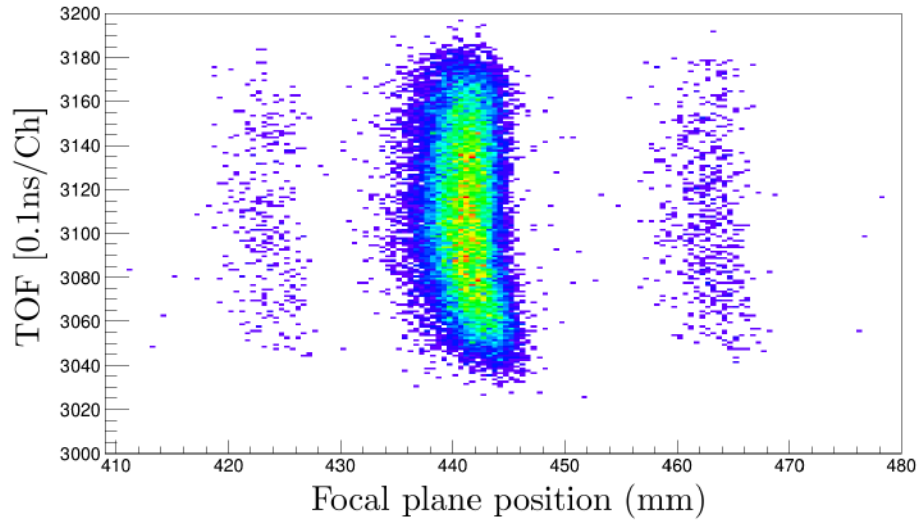
Figure 4.16: *Zoom-in of TOF versus the focal plane position before the lineshape correction.*
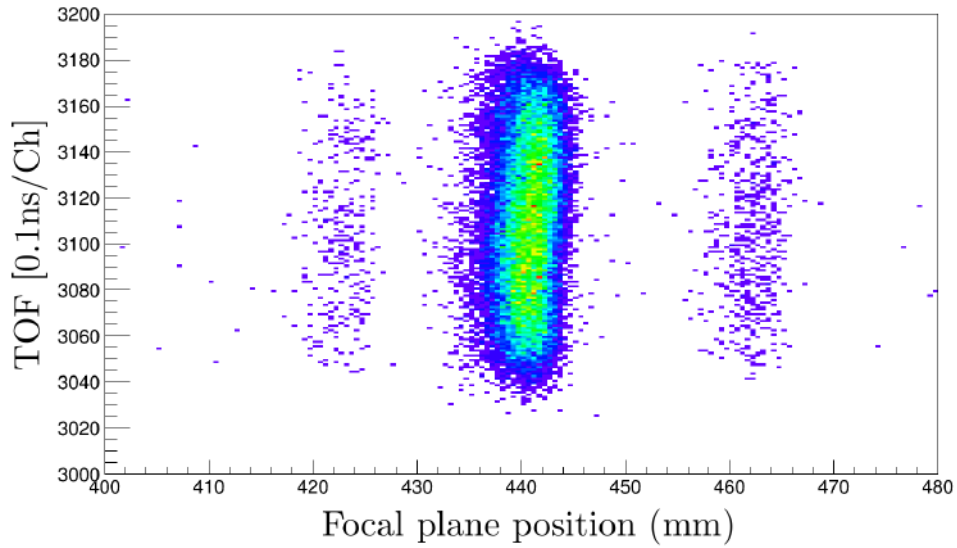
Figure 4.17: *Zoom-in of TOF versus the focal plane position after the lineshape correction.*
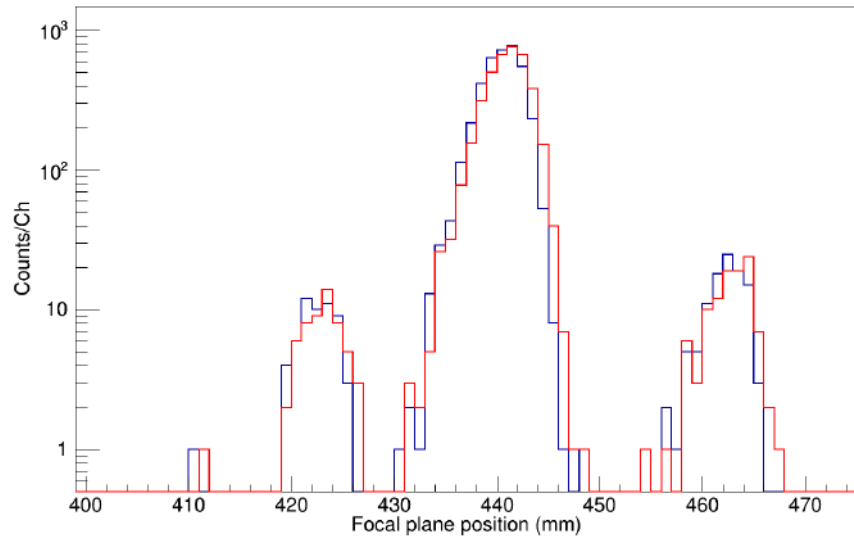
Figure 4.18: *Zoom-in of one-dimensional focal plane position spectra of calibration reaction* ^{26}Al *before (blue) and after (red) linear correction.*
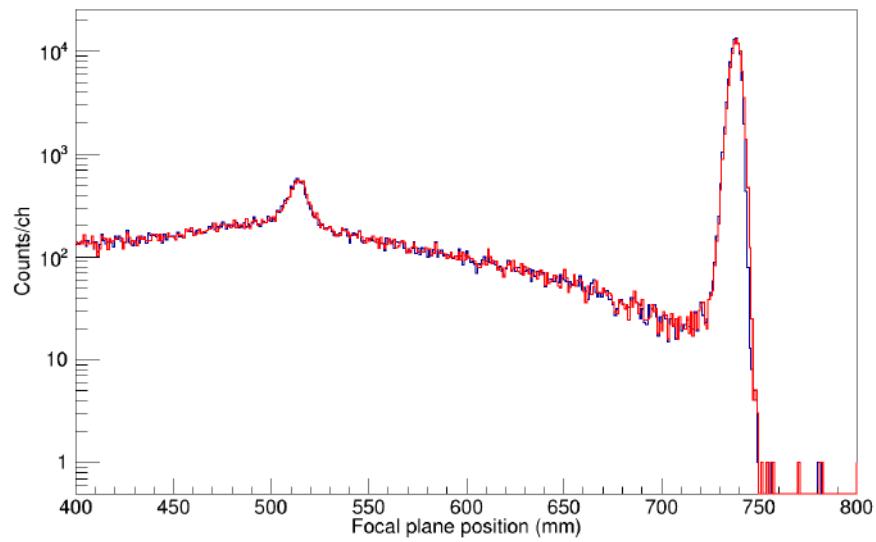
Figure 4.19: *Zoom-in of one-dimensional focal plane position spectra of calibration reaction* ^{9}B *before (blue) and after (red) linear correction.*

61

4.6   Focal Plane Calibration

I now describe the energy calibration procedure for the focal plane spectra, corresponding to both the high and low excitation energy regions in ^{9}B. As mentioned in Section 4.1, the PID spectra were used to generate the focal plane (position) spectra for both cases. For the high excitation energy region we could not detect tritons from ^{26}Mg(^{3}He,t) reactions that could be used for an energy calibration (with the same spectrometer field settings).
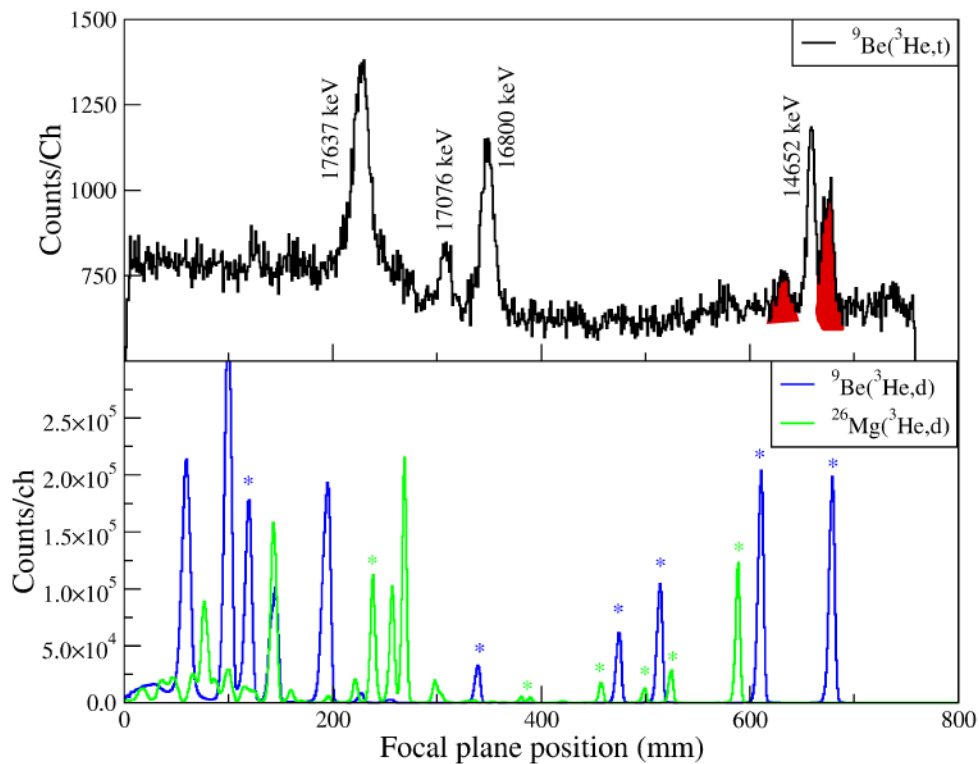
Figure 4.20: *Top panel: Triton spectrum from ^{9}Be(^{3}He,t)^{9}B reaction in the 14-18 MeV excitation region.   Bottom Panel: Calibration spectra obtained from ^{9}Be(^{3}He,d)^{10}B and ^{26}Mg(^{3}He,d)^{27}Al reactions. Only the peaks marked with asterisks were used for the energy calibration. The shaded peaks are potential new states identified from this experiment. These are discussed briefly in the next chapter.*
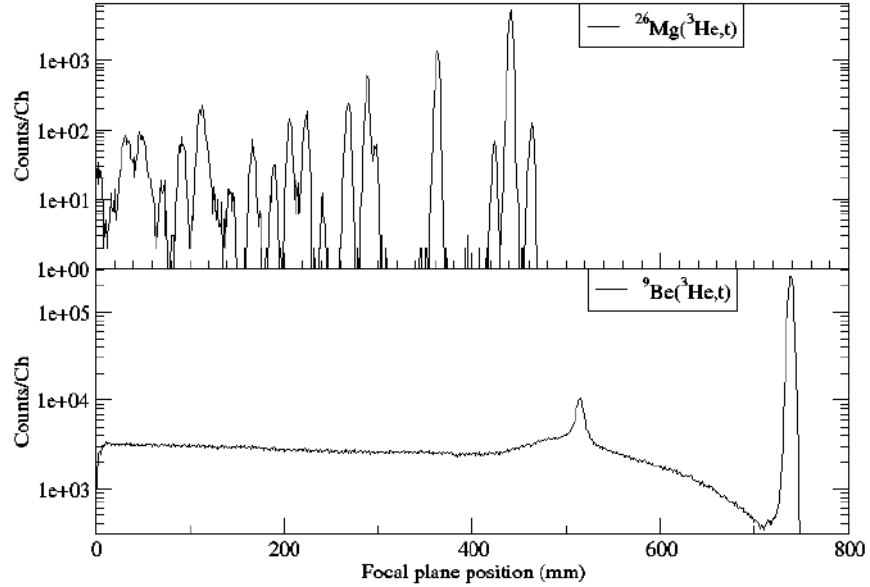
Figure 4.21: *Top panel: Calibration spectrum from* $^{26}\mathrm{Mg}(^{3}\mathrm{He}, t)^{26}\mathrm{Al}$ *reactions. Bottom Panel: Triton spectrum from* $^{9}\mathrm{Be}(^{3}\mathrm{He}, t)^{9}\mathrm{B}$ *reaction in the 0-4 MeV excitation region.*

However, in this case we take advantage of $^{9}\mathrm{Be}(^{3}\mathrm{He}, d)$ and $^{26}\mathrm{Mg}(^{3}\mathrm{He}, d)$ reaction deuterons to perform an energy calibration of the tritons from $^{9}\mathrm{Be}(^{3}\mathrm{He}, t)$. As shown in the upper panel of Fig 4.20, the triton spectrum has considerable overlap with deuteron spectra obtained using the same spectrometer field settings, for both the $^{9}\mathrm{Be}$ and $^{26}\mathrm{Mg}$ targets.

In the low excitation energy region, one type of charged particles (tritons) were detected at the focal plane. The PID gates corresponding to the tritons groups were used to generate the $^{26}\mathrm{Mg}(^{3}\mathrm{He}, t)^{26}\mathrm{Al}$ and $^{9}\mathrm{Be}(^{3}\mathrm{He}, t)^{9}\mathrm{B}$ position spectra, as shown in Fig. 4.21. The former were used to calibrate the tritons from $^{9}\mathrm{Be}(^{3}\mathrm{He}, t)$, corresponding to the low lying excitation region of $^{9}\mathrm{B}$.

In the following, I first discuss the analysis of the data for the high excitation region, high-lighted by the triton peaks in Fig. 4.20. I elucidate the procedure used to remeasure the excitation energy of the $E_x \approx 17076$ KeV state, which was clearly populated with the $^9\mathrm{Be}(^3\mathrm{He}, t)$ reaction and identified in Fig. 4.20. I defer the discussion on the fit procedure to obtain the energy of the first $\frac{1}{2}^+$ excited state (which is part of the continuum in the lower panel of Fig. 4.21) to Section 4.7. This is mainly because the low energy region is dominated by broad interfering resonances.

On the other hand, the focal plane spectra shown in Fig. 4.20 were fitted using the Levenberg-Marquardt χ^2 minimization routine described previously. For these spectra we observe that the energy resolution of the spectrometer was comparable to (or worse than) the intrinsic widths of the states that are highlighted. This feature allowed us to fit the triton peaks using a simple function that consisted of a Gaussian on a flat background. Since the spectrometer was optimised for the $(^3\mathrm{He}, t)$ reaction, the deuteron peaks required a different fit function, whose lineshape was the convolution of a Gaussian with a low energy tail. This is not surprising, considering that the reactions had different kinematics. Some of the fits are shown in Fig. 4.22. Once the peak centroids were determined, the focal plane spectra were energy calibrated following a procedure that used another iterative algorithm, which is described below. The first step in this procedure was to obtain the corrections due to energy losses for both deuterons and the tritons within the target foils. The algorithm used a similar approach to the one used to obtain the target thicknesses. Similarly as in section 4.4, we start off with an energy loss interpolation, which was performed using the stopping powers $(\frac{dE}{dX})$ for deuterons and tritons within $^{26}\mathrm{Mg}$ and $^9\mathrm{Be}$ at energies ranging from approximately 10 to 70 MeV. These values were obtained from SRIM and shown in Figs. 4.23 and 4.24. The stopping powers were then fitted to a polynomial function of order 4, which allowed a determination of ejectile energy losses for arbitrary values of energies. The next step was to generate the momentum distribution for the deuterons from both calibration targets using Monte Carlo simulations. This is because of the reasonably large thickness of the foils. The
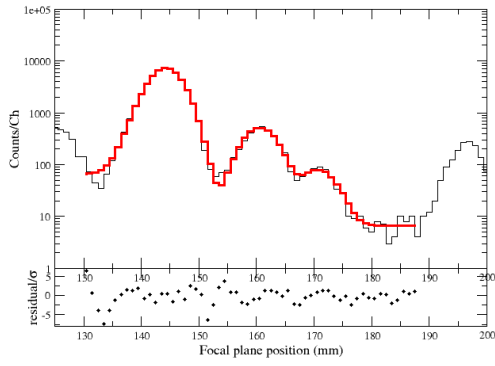
(a)
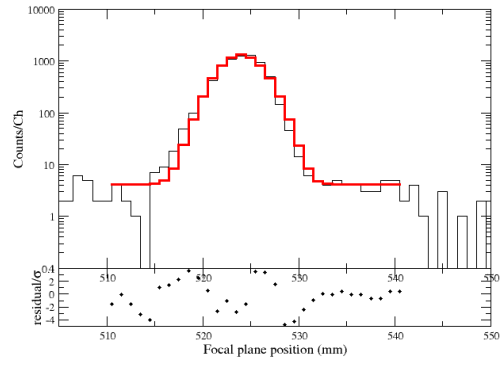
(b)
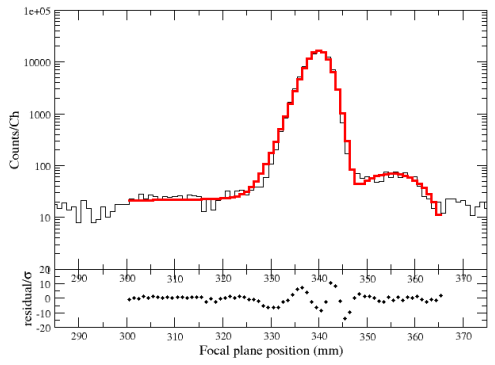
(c)
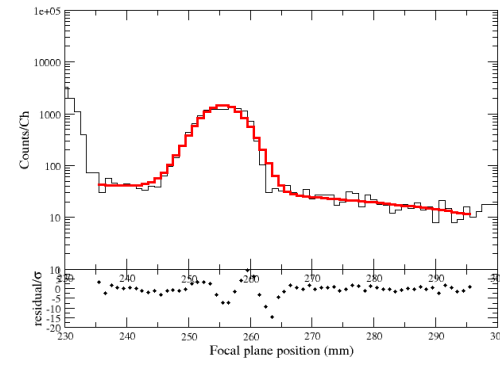
(d)

Figure 4.22: Fits to the deuteron peaks from both ^{9}Be(^{3}He, d)^{10}B and ^{26}Mg(^{3}He, d)^{27}Al reactions.

simulations assumed a uniform probability distribution for the location of the reactions in the targets, assuming the location to be a random variable

$$X = rndm \times t, \tag{4.11}$$

where $rndm$ is a uniform random number generated between 0 and 1, and t is the target thickness. Once a random reaction location was chosen, the energy loss of the incident ^{3}He beam was calculated for that location using a similar iterative algorithm as Fig. 4.14. After traversing a linear distance X, the energy loss of the incoming beam would be

$$E_{loss} = \int_0^X dX \ (dE/dX)_E. \tag{4.12}$$

The above integration was performed numerically by dividing the targets into infinitesimal slices and further assuming the energy loss (dE/dX) to be constant over each slice. The (dE/dX) values for each value of E were obtained from the polynomial fits shown in Figs. 4.23 and 4.24. Once the reduced energies for the projectile were determined, these values were fed into relativistic kinematics code to obtain the energies of the ejectiles at $0°$.
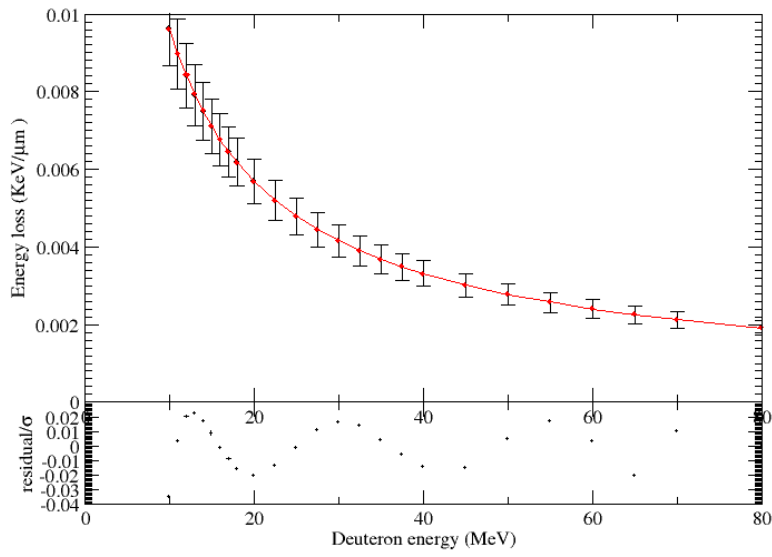
Figure 4.23: *Fit to the energy loss as a function of deuteron energy for* ^{26}Mg *target.*
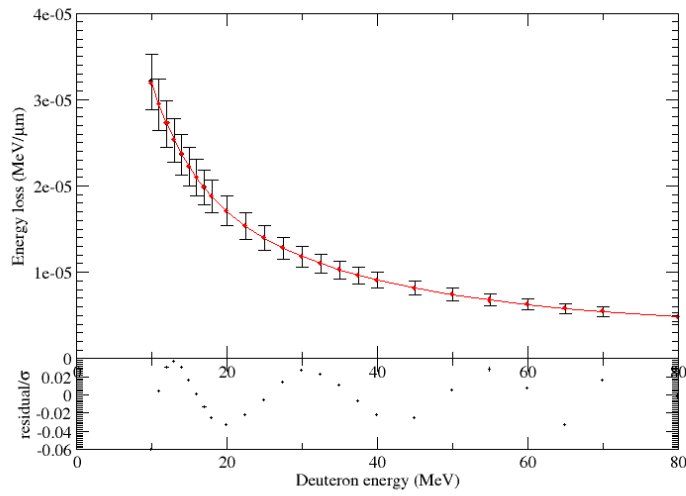
Figure 4.24: *Fit to the energy loss as a function of deuteron energy for* ^{9}Be *target.*
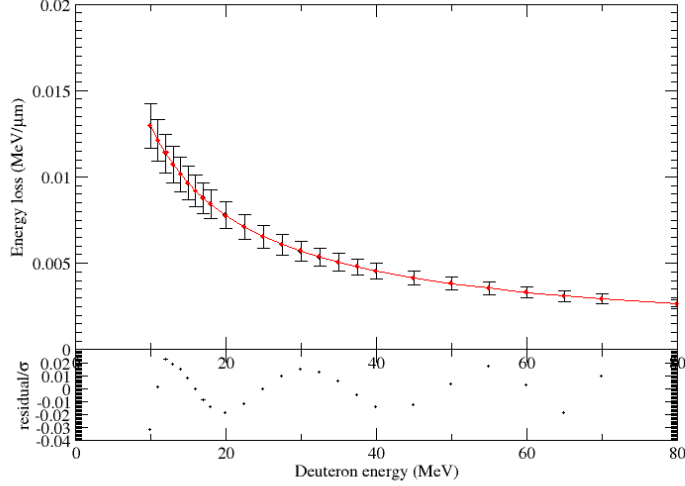
Figure 4.25: *Fit to the energy loss as a function of triton energy for* ^{9}Be *target.*

Next, a similar procedure was used to account for ejectile energy loss through the remainder of the target. The final momenta for the simulated outgoing ejectiles at the focal plane were histogrammed as shown in Fig. 4.26. This histogram shows that the momenta also had a uniform distribution, similar to the uniform probability density function describing the location of the reactions in the target. This similarity allowed us to assume that the average momenta for the calibration deuterons were simply

$$\bar{p}_d(i) = \frac{p_{min}(i) + p_{max}(i)}{2},\tag{4.13}$$

where $p_{min}(i)$ and $p_{max}(i)$ correspond to reactions on the back and the face of the target respectively. The uncertainties to these averaged values are [68]

$$\sigma(i) = \sqrt{\frac{(p_{max}(i) - p_{min}(i))^2}{12}}.\tag{4.14}$$

68
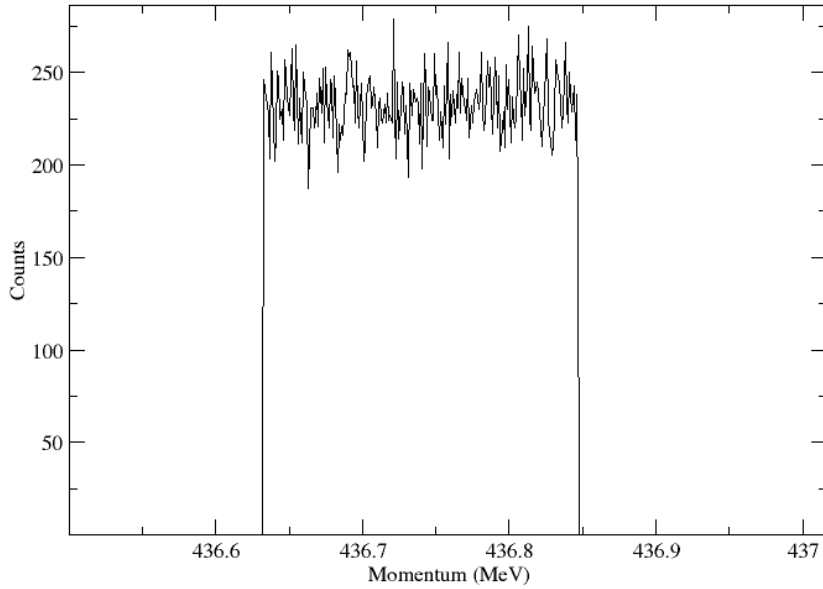
Figure 4.26: *The momentum distribution for deuterons from* $^9\mathrm{Be}(^3\mathrm{He}, d)$.

Figure 4.27 shows a flow chart of the iterative procedure described above. Further Monte Carlo simulations were performed for all concerned reactions, under the assumption that they take place at the centre of the targets. The above means that statistically (on average) it is safe to assume that all the reactions took place at the center of the target.
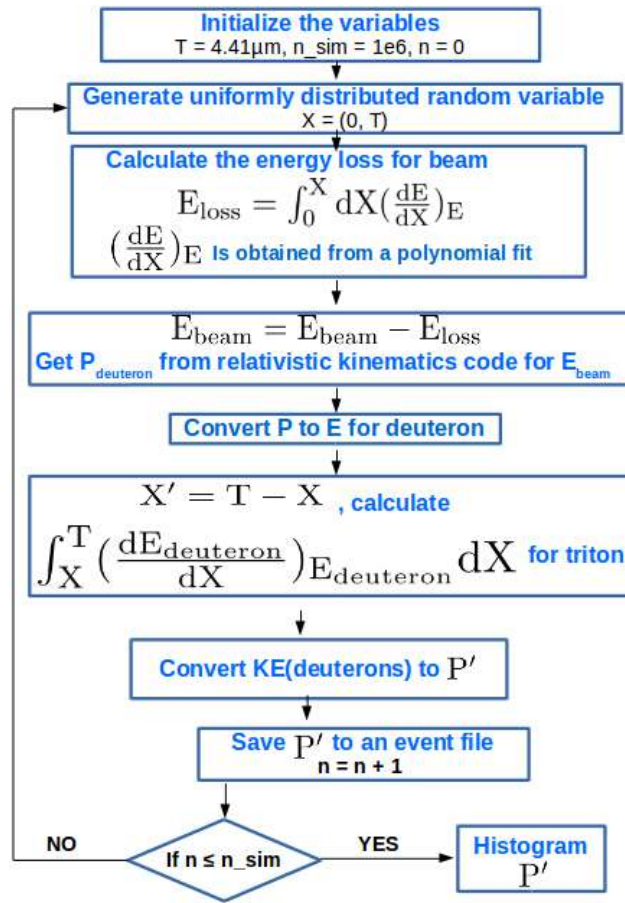
Figure 4.27: *Monte carlo simulation procedure. Here, T is the target thickness, n_sim is the total number of simulations.*

In the final step of the calibration, the $\bar{p}_d(i)$ values corresponding to well known and identified excited states in ^{10}B and ^{27}Al (shown in Fig. 4.20) were determined using similar corrections for energy losses. These calibrated the ejectile momenta at the focal plane of the spectrometer. In Tables 4.2 and 4.3 I show the data that were used for the focal plane calibration using this procedure.

Table 4.2: Centroids of focal plane positions for deuteron peaks correspondidng to ^{10}B excited states, their corresponding averaged momenta and associated unccertainties.

$\mu(i)$	$\Delta\mu(i)$	$\bar{P_d}(i)$	$\Delta\bar{P_d}(i)$
682.016	0.022	441.141	4.570E-06
613.225	0.973	437.843	5.072E-05
516.441	0.008	433.101	0.0001
477.150	0.010	431.160	0.002
341.024	0.013	424.363	0.002
228.740	0.237	418.631	0.002

Table 4.3: Centroids of deuteron peaks corresponding to well identified levels in ^{27}Al, their corresponding averaged momenta and associated uncertainties.

$\mu(i)$	$\Delta\mu(i)$	$\bar{P_d}(i)$	$\Delta\bar{P_d}(i)$
589.769	0.012	436.740	2.243e-04
524.780	0.024	433.595	4.069e-03
499.344	3.75e-02	432.342	1.814e-03
457.815	0.031	430.282	1.823e-03
389.638	0.067	426.870	3.677e-03
381.151	0.062	426.445	2.760e-03
335.396	0.099	424.122	4.627e-03
328.549	0.141	423.773	3.705e-03
298.692	0.052	422.235	3.254e-03
238.863	1.54e-02	419.144	6.090e-03

Finally, the focal plane calibration was performed using a quadratic fit to the peak centroids $\mu(i)$,

$$\bar{p}_d(i) = a_0 + a_1\mu(i) + a_2\mu(i)^2. \tag{4.15}$$

The results from our $^9\mathrm{Be}(^3\mathrm{He}, d)$ and $^{26}\mathrm{Mg}(^{3\mathrm{He}}, d)$ calibrations are shown in Figs. 4.28 and 4.29. The a_0, a_1, and a_3 calibration coefficients were used to convert the $^9\mathrm{Be}(^3\mathrm{He}, t)$ peak centroids to triton momenta.
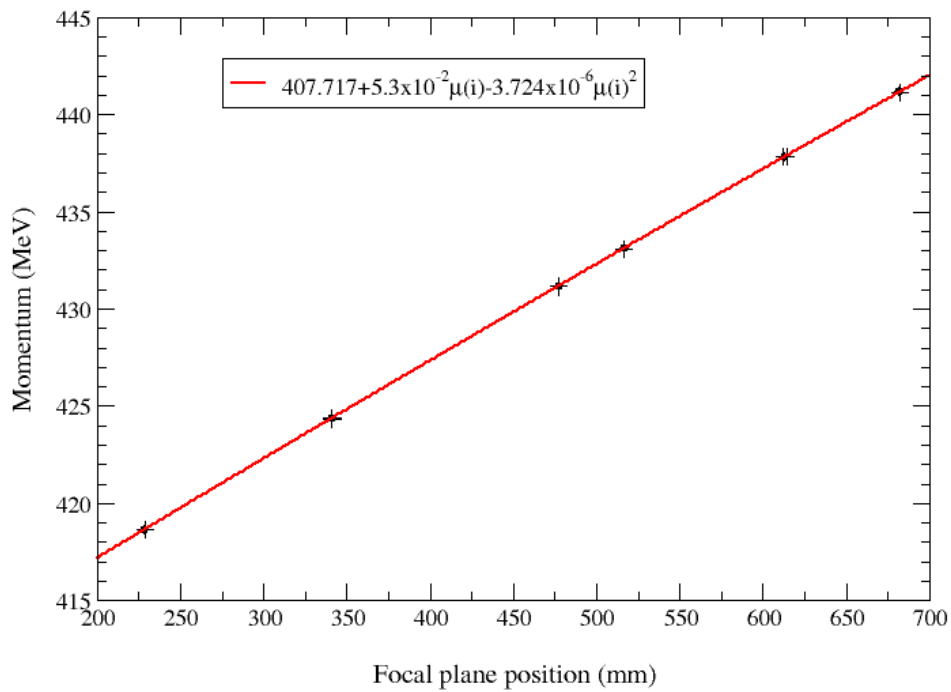
Figure 4.28: *Second order polynomial fit of $\bar{P}_d(i)$ versus $\mu(i)$ for the $^9\mathrm{Be}(^3\mathrm{He}, d)^{10}\mathrm{B}$ reaction.*
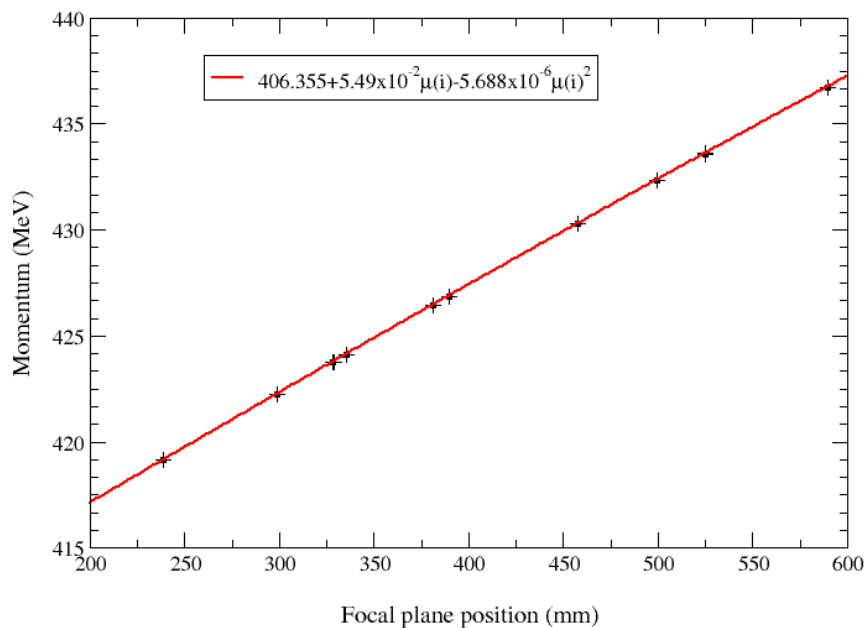
Figure 4.29: *Second order polynomial fit $\bar{P}_d(i)$ versus $\mu(i)$ for the ^{26}Mg(^{3}He, d)^{27}Al reaction.*

The final step in the analysis was to correct for these momentum values (again assuming that the reactions occurred at the center of the ^{9}Be target) for the energy loss differences between the deuterons and the tritons. Final ^{9}B excitation energies were back calculated using these corrected momenta and the relativistic kinematics code. Our extracted results are shown in Table 4.4. The estimations of systematic uncertainties contributing to these measurements are discussed in the next section.

Table 4.4: ^{9}B excitation energies in the 14-18 MeV obtained from both calibration reactions. The final energies are from a weighted mean of the results from both calibrations.

^{9}Be$(^3$He$, d)^{10}$B calibration (keV)	^{26}Mg$(^3$He$, d)^{27}$Al calibration (keV)	$E_x(^9$B) (keV)
14538 ± 2	14538 ± 2	14538 ± 19
14583 ± 4	14582 ± 4	14582 ± 19
14665 ± 1	14663 ± 1	14664 ± 19
14847 ± 3	14842 ± 3	14845 ± 19
16795 ± 1	16790 ± 1	16792 ± 19
17074 ± 3	17071 ± 3	17073 ± 19
17627 ± 1	...	17627 ± 19
18329 ± 5	...	18329 ± 20

4.6.1 Calculation of systematic uncertainties in the determined excitation energies

The systematic uncertainties in the extracted excitation energies of ^{9}B were calculated using 1σ shifts in beam energy, target thickness, Q-values, stopping powers, energy losses from SRIM and the calculated average ejectile momenta. The dominant uncertainty arises from the beam energy which had an uncertainty of ± 50 keV, which arises from a conservative estimate of the bending radius of the analysing magnet that is located upstream of the K600 spectrometer. The results of relative uncertainties from systematic effects in the determination of the excitation energy of the second $T = 3/2$ state in ^{9}B are shown in Table 4.5.

Table 4.5: Relative contributions of systematic uncertainties in our determination of the excitation energy of the second $T = 3/2$ state in ^{9}B.

Source of uncertainty	$\Delta E_x/E_x$ [%]
Ground state masses	0.004
Beam energy	0.092
Target thickness	0.01
Ejectile momenta ($\bar{p}_d$) used for calibration	0.05
Stopping powers	0.008
Total	0.11

4.7 Analysis of spectra covering the low lying excitation region in ^{9}B

The low lying excitation region in such light nuclei are dominated by particle unbound states that have large widths. Consequently ^{9}Be(^{3}He, t) the triton spectrum in this region is composed of several wide overlapping peaks, that need to be deconvoluted from one another. In order to achieve this, we use a lineshape fitting program called ALLFIT that was specially developed to fit complicated spectra containing multiple peaks with complicated backgrounds with continuum shapes [69–71]. The code uses a fitting function

$$y(x) = \epsilon(x)[B(x) + \sum_{i=1}^{N} y_i(x)] \tag{4.16}$$

where ϵ is an efficiency function (which we set to unity), $B(x)$ is a background function, and the summation is over N individual peaks represented by $y(i)$. The lineshape of each peak is the convolution of an intrinsic lineshape $I(x)$ and a resolution function $R(x)$ written

symbolically as

$$y(x) = I_i \otimes R. \tag{4.17}$$

For narrow peaks, whose intrinsic widths are much smaller than the detector resolution, the peak shapes reduce to just $y_i(x) = R(x)$. The convolutions in ALLFIT [?] are carried out using a fast Fourier transform (FFT) routine. For spectrometer experiments, the shape of the resolution function in ALLFIT depends on projectile kinematics in the laboratory frame, and is given by

$$R(i) = R(x_i)dx_i, \tag{4.18}$$

where x_i is the appropriate kinematic variable and dx_i is the width of channel i with respect to x. Quite obviously, for K600 spectrometer data, x would be the laboratory momentum for the projectile. There are two lineshape resolution functions that can be invoked by the code. One is a simple asymmetric Gaussian, while the other is an asymmetric hyperGaussian with both low and high energy exponential tails. The former is a special case of the latter, which has a more complicated lineshape. For our analysis we assumed the peak lineshape resolution function to be the asymmetric hyperGaussian, which can be more or less pointed than a normal distribution, depending on an exponent parameter γ. The hyperGaussian function is described in greater detail in Ref [69]. We also assume an intrinsic lineshapes for the peaks to have functional forms, defined by Breit-Wigner function

$$I(Q) = \frac{A(\Gamma/2)^2}{(Q - Q_0)^2 + \Gamma^2/4} \tag{4.19}$$

where Q_0 is a position parameter that is related to the Q value, A is the amplitude (peak height) and Γ is the intrinsic width of the state. The background was assumed to be of the form of a cubic function

$$B(x_i) = b_0 + b_1 x_i + b_2 x_i^2 + b_3 x_i^3, \tag{4.20}$$

where x_i is the appropriate kinematic variable (in this case the laboratory momentum of the projectile), given a particular reaction Q value.

4.7.1 Results of the deconvolution using ALLFIT

As shown in Figs. 4.20 and 4.21, the focal plane position spectra for spectrometer experiments display the higher energy ejectiles (corresponding to lower excitation energy) at higher channels, due to rigidity considerations. Consequently, the peaks corresponding to lower excitation energy appear at higher channel numbers. In order to provide a meaningful input file for ALLFIT, it is first required to invert these spectra, so that peaks corresponding to lower excitation energies appear on the left of the spectrum and vice versa. Therefore the first step in this part of the analysis was to invert the $^{26}\mathrm{Mg}(^3\mathrm{He},t)^{26}\mathrm{Al}$ and $^9\mathrm{Be}(^3\mathrm{He},t)^9\mathrm{B}$ focal plane spectra shown in Fig. 4.21. The flipped spectra are shown in Fig. 4.30. Since the $^{26}\mathrm{Mg}(^3\mathrm{He},t)$ spectrum consisted of distinct narrow peaks, similar to the high excitation $^9\mathrm{B}$ region and deuteron peaks shown in Fig.4.20, we used the same fitting routine described in Sections 4.4 and 4.6 to obtain their peak centroids. Some characteristic fits to the triton focal plane calibration spectrum are shown in Fig. 4.31.

As apparent from Fig. 4.30, the calibration requires a significant extrapolation to cover the entire $^9\mathrm{B}$ excitation region of interest. We therefore use the triton peak corresponding to the ground state of $^9\mathrm{B}$ as an additional calibration point. A similar iterative algorithm (as shown in Fig. 4.27) was used to calibrate the tritons from $^9\mathrm{Be}(^3\mathrm{He},t)$, after a careful consideration of corrections due to energy losses for tritons within the target foils. The $\bar{p}_t(i)$ values corresponding to well known and identified excited states in $^{26}\mathrm{Al}$ (shown in the top panel Fig. 4.30) were then determined.
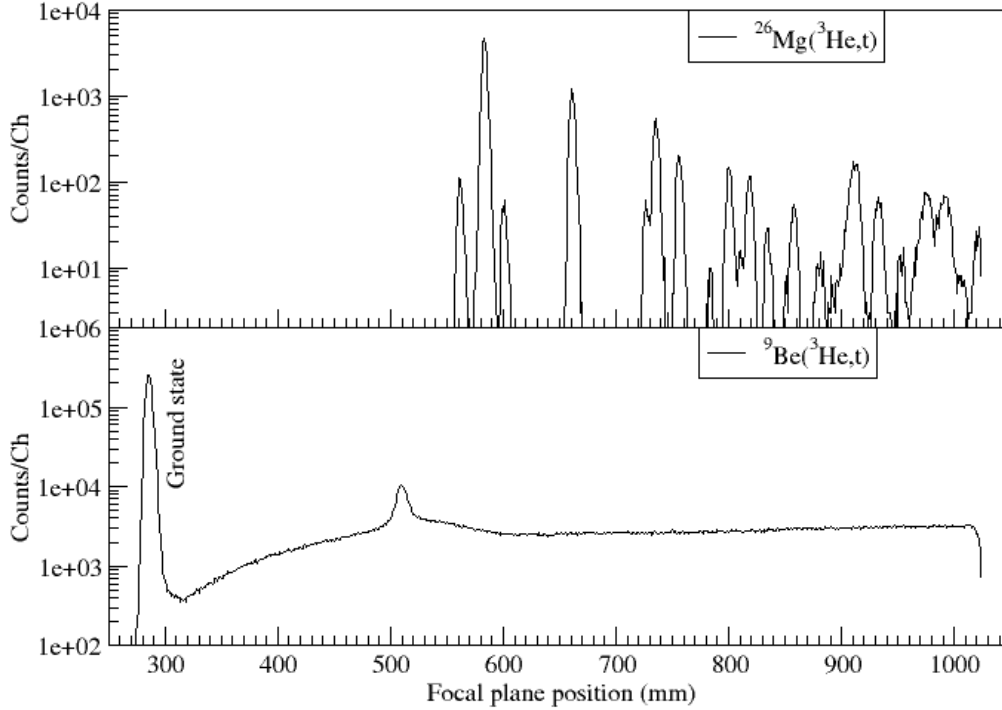
Figure 4.30: *Top panel: Inverted calibration spectrum obtained from the* $^{26}\text{Mg}(^3\text{He},t)^{26}\text{Al}$ *reaction. Bottom Panel: The inverted triton spectrum from the* $^9\text{Be}(^3\text{He},t)^9\text{B}$ *reaction in the 0-4 MeV excitation region.*

These were used to calibrate the ejectile momenta at the focal plane of the spectrometer. Table 4.6 lists the data that we used for the focal plane calibration. The centroid of the ground state peak in ^9B was obtained from ALLFIT (see Fig. 4.33) and included in the calibration as well. The calibration coefficients obtained from a second order polynomial fit is shown in Fig. 4.32. These coefficients are eventually used to convert the deconvoluted $^9\text{Be}(^3\text{He},t)$ peak centroids into triton momenta.

(a)

(b)
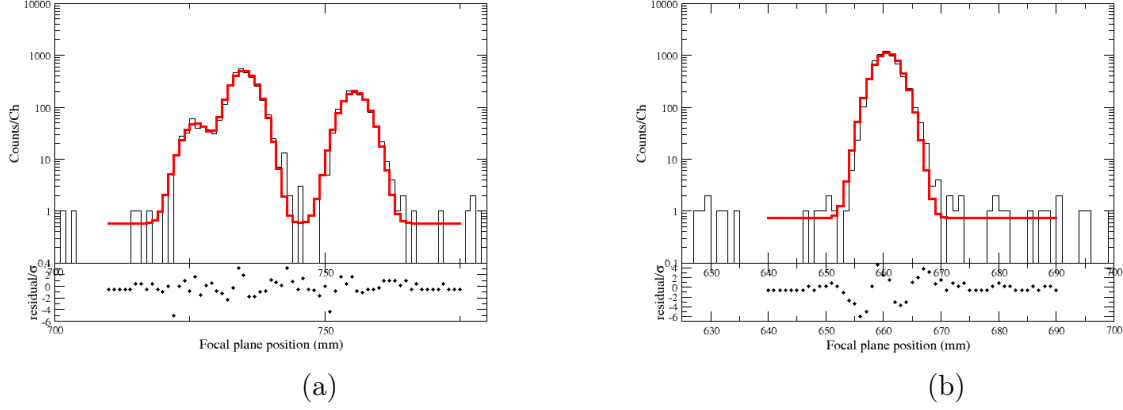
Figure 4.31: *Fits to selected triton peaks from* $^{26}\text{Mg}(^3\text{He}, t)^{26}\text{Al}$ *reaction.*

Table 4.6: Centroids of focal plane positions for triton peaks corresponding to the ^9B ground state and other $^{26}\text{Mg}(^3\text{He}, t)^{26}\text{Al}$ excited states, their corresponding average momenta, and associated unccertainties.

$\mu(i)$	$\Delta\mu(i)$	$\bar{P_d}(i)$	$\Delta\bar{P_d}(i)$
285.103	0.025	529.604	7.818E-05
561.663	0.101	513.540	8.065E-05
583.244	0.014	512.262	2.103E-05
600.924	0.139	511.205	4.863E-06
661.181	0.028	507.592	1.960E-5
726.712	0.175	503.606	1.318E-05
735.533	0.044	503.083	4.949E-05

79
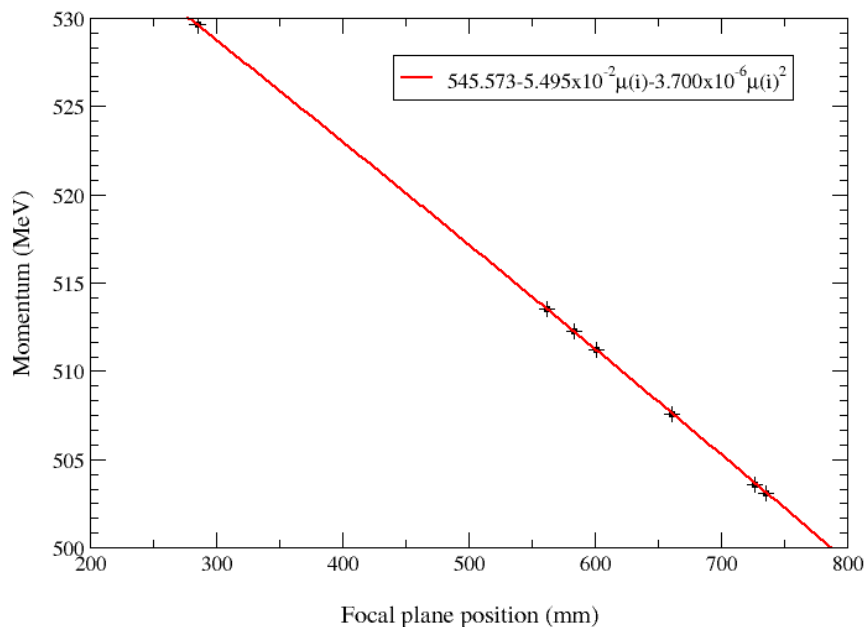
Figure 4.32: *Second order polynomial fit of $\bar{P}_d(i)$ versus $\mu(i)$ for the ^{26}Mg$(^3$He$, t)^{26}$Al reaction.*

The final result for the excitation energy of the first $\frac{1}{2}^+$ state in ^{9}B is shown in Table 4.7, after taking into consideration all systematic uncertainties. Fig. 4.34 and 4.33 show the fitted results on using ALLFIT. The fit does not yield the best $\chi^2/\nu(\chi^2/\nu \approx 3.2)$, but we are still working on certain refinements to the fitting procedure. Nevertheless, we obtain nice agreement with energy of the 2.3 MeV state in comparison with the ENSDF database on NNDC [25].

Table 4.7: ^{9}B excitation energies obtained using the ^{26}Mg$(^3$He$, t)^{26}$Al calibration reaction.

^{26}Mg$(^3$He$, t)^{26}$Al calibration (keV)	$E_x(^9$B$)$ (keV)	NNDC
0	0	0
1864 ± 1	1864 ± 15	$\approx 1500?$
2354 ± 3	2354 ± 13	2345 ± 11
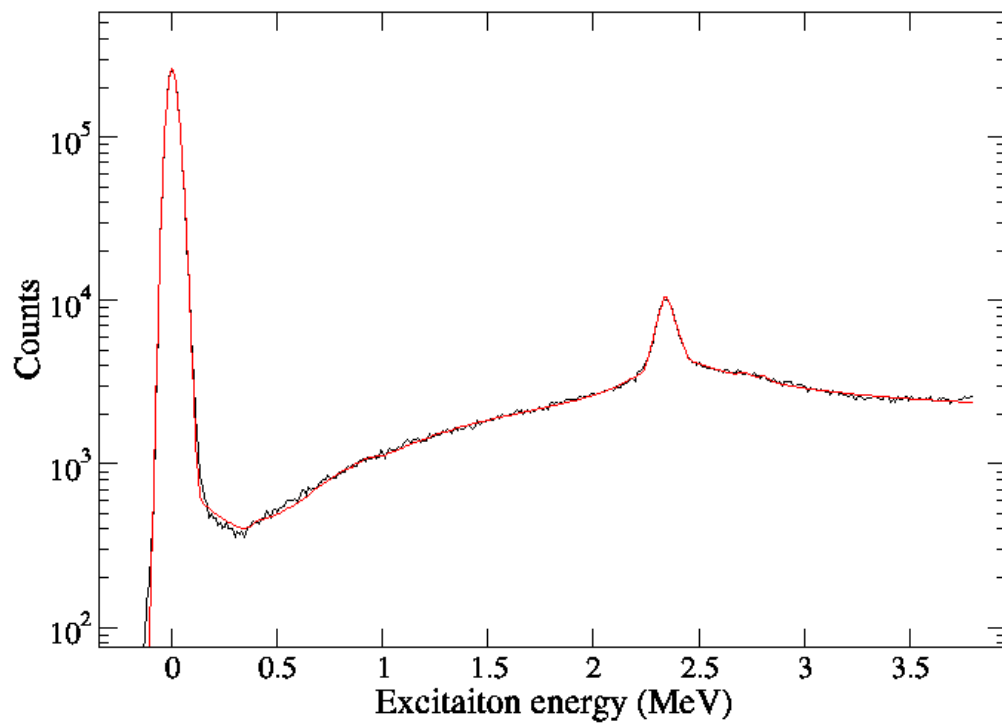
Figure 4.33: *Calibrated* ^{9}Be(^{3}He, t) *spectra. The red overlay shows the fit to the data using ALLFIT.*
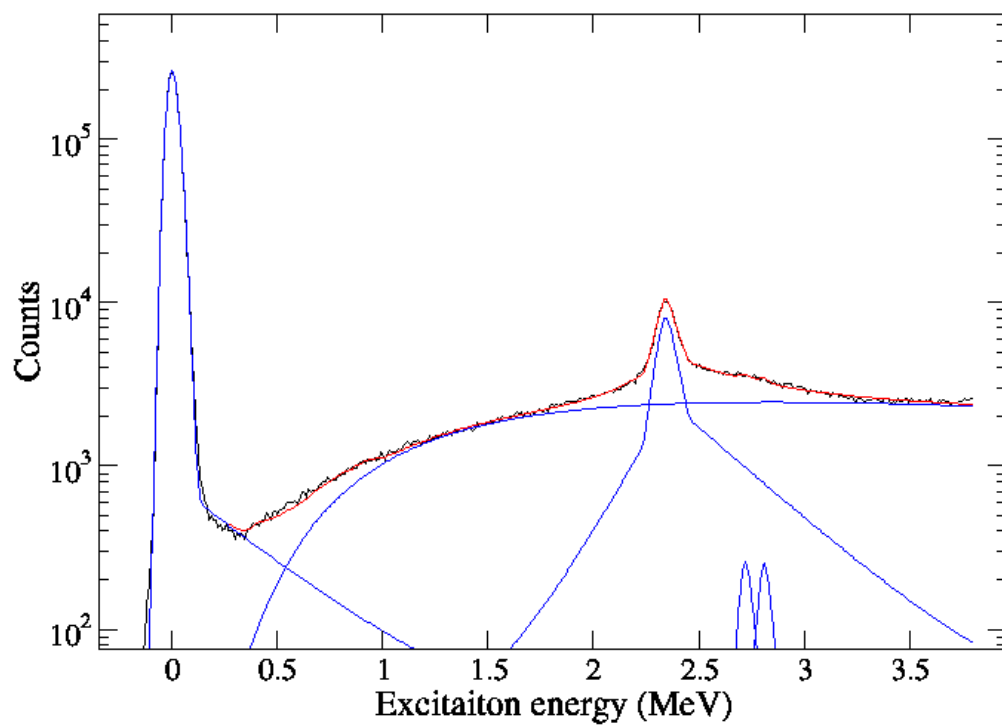
Figure 4.34: *Calibrated* ^{9}Be(^{3}He,t) *spectra. The red overlay shows the fit to the data using* *ALLFIT.*

CHAPTER 5

CONCLUSIONS

In conclusion, we performed spectroscopy both the high lying and as well as low lying excitation region of the light unbound nucleus ^{9}B using the ^{9}Be(^{3}He, t) reaction with the K600 spectrometer at iThemba LABS. We identify four new tentative states in ^{9}B, which are not included in the lastest compilation of $A = 9$ nuclei. The chances that these peaks arise from ^{12}C and ^{16}O contaminants are minuscule due to the large differences in reaction Q values for these contaminants. Our determination of the energy of the second $T = 3/2$ state in ^{9}B agrees with the older ^{11}B(p, t) measurement [29] while differing significantly from the most recent measurement done by Charity *et al* [23]. We thereby rule out the longstanding hypothesis that the requirement of a large cubic term to the IMME for the first $A = 9$, $T = 3/2$ quartet is mainly due to coupling of the least-bound proton in ^{9}C with the particle continuum [24, 72]. Clearly, if continuum coupling were the main reason for the IMME violation, then the deviation from the quadratic IMME would be much worse for the second $T = 3/2$ quartet, where the proton separation energies are much smaller. We do not observe this. We also agree with the shell model predictions of Brodeur *et al* [22] that indicated no significant isospin mixing in the excited quartet. Our findings have been accepted for publication as a Rapid Communication with Physical Review C [73].

We also used the ALLFIT code to deconvolute the low energy ${}^{9}\text{Be}({}^{3}\text{He}, t)$ spectrum in order to determine precisely the excitation energy of the $\frac{1}{2}^{+}$ state in ${}^{9}\text{B}$ for comparison with theoretical predictions. Our result is in agreement with [39, 52, 53] indicating excellent agreement with the R-matrix calculations of Barker [43], while significantly disagreeing with microscopic cluster model and single particle potential model estimates.

BIBLIOGRAPHY

[1] E. M. Henley and A. Garcia, *Subatomic physics*. World Scientific, 2007.

[2] S. M. Lenzi, "Coulomb energy differences in mirror nuclei," in *Journal of Physics: Conference Series*, vol. 49, p. 85, IOP Publishing, 2006.

[3] K. Kaneko, T. Mizusaki, Y. Sun, S. Tazaki, and G. de Angelis, "Coulomb Energy Difference as a Probe of Isospin-Symmetry Breaking in the Upper f p-Shell Nuclei," *Physical Review letters*, vol. 109, no. 9, p. 092504, 2012.

[4] D. H. Wilkinson, *ISOSPIN IN NUCLEAR PHYSICS*. North-Holland, Amsterdam, 1969.

[5] R. Casten and R. F. Casten, *Nuclear structure from a simple perspective*, vol. 23. Oxford University Press, 2000.

[6] M. Bentley *Physical Review C*, vol. 92, p. 024310, 2015.

[7] B. Agrawal, T. Sil, S. Samaddar, J. De, and S. Shlomo, "Coulomb energy differences in mirror nuclei revisited," *Physical Review C*, vol. 64, no. 2, p. 024305, 2001.

[8] R. G. Thomas *Physical Review*, vol. 88, p. 1109, 1952.

[9] J. B. Ehrman, "On the displacement of corresponding energy levels of ^{13}C and ^{13}N," *Physical Review*, vol. 81, no. 3, p. 412, 1951.

[10] D. J. M. Lámbarri. PhD thesis, The University of Birmingham, (2015).

[11] K. Krane, *Introductory Nuclear Physics*. Wiley & Sons, (1988).

[12] D. J. Rowe and J. L. Wood, *Fundamentals of nuclear models: foundational models.* World Scientific Publishing Company, 2010.

[13] I. Ragnarsson and S. G. Nilsson, *Shapes and shells in nuclear structure.* John Wiley & Sons, Inc.,New York,, 1961.

[14] P. J. Brussaard and P. W. M. Glaudemans, *Shell-model applications in nuclear spectroscopy.* North-Holland Pub. Co., 1977.

[15] B. A. Brown, "Lecture notes in nuclear structure physics," *National Super Conducting Cyclotron Laboratory*, 2005.

[16] W. Fairbairn, "The coulomb energies of the lower excited levels in the light mirror nuclei," *Nuclear Physics*, vol. 45, pp. 437–442, 1963.

[17] J. Carlson, S. Gandolfi, F. Pederiva, S. C. Pieper, R. Schiavilla, K. E. Schmidt, and R. B. Wiringa, "Quantum monte carlo methods for nuclear physics," *Reviews Modern Physics*, vol. 87, pp. 1067–1118, Sep 2015.

[18] W. Von Oertzen, "Two-center molecular states in ^{9}B,^{9}Be,^{10}Be, and ^{10}B," *Z. Phys. A*, vol. 354, pp. 37–43, 1996.

[19] J. Kroepfl and C. Browne, "Energy level structure of ^{9}Be and ^{9}B," *Nuclear Physics A*, vol. 108, no. 2, pp. 289–315, 1968.

[20] F. Lauritsen and F. Ajzenberg-Selove, "Energy Levels of Light Nuclei $A = 5 - 10$," *Nuclear Physics*.

[21] M. MacCormick and G. Audi, "Evaluated experimental isobaric analogue states from $T = 1/2$ to $T = 3$ and associated imme coefficients," *Nuclear Physics A*, vol. 925, pp. 61–95, 2014.

[22] M. Brodeur, T. Brunner, S. Ettenauer, A. Lapierre, R. Ringle, B. Brown, D. Lunney, and J. Dilling, "Elucidation of the anomalous $A = 9$ isospin quartet behavior," *Physical review letters*, vol. 108, no. 21, p. 212501, 2012.

[23] R. J. Charity, J. M. Elson, J. Manfredi, R. Shane, L. G. Sobotka, B. A. Brown, Z. Chajecki, D. Coupland, H. Iwasaki, M. Kilburn, *et al.*, "Investigations of three-, four-, and five-particle decay channels of levels in light nuclei created using a ^{9}C beam," *Physical Review C*, vol. 84, no. 1, p. 014320, 2011.

[24] G. Bertsch and S. Kahana *Physics Letters B*, vol. 33, p. 193, 1970.

[25] "www.nndc.bnl.gov."

[26] R. Julies, W. Richter, and B. Brown, "The $0p$ shell revisited," *South African Journal of Physics*, vol. 15, p. 35, 1992.

[27] B. Brown *Progress in particle and Nuclear Physics*, vol. 47, p. 517, 2001.

[28] R. J. Charity, J. M. Elson, J. Manfredi, R. Shane, L. G. Sobotka, B. A. Brown, Z. Chajecki, D. Coupland, H. Iwasaki, M. Kilburn, *et al.*, "Investigations of three-, four-, and five-particle decay channels of levels in light nuclei created using a ^9C beam," *Physical Review C*, vol. 84, no. 1, p. 014320, 2011.

[29] W. Benenson and E. Kashy, "First excited $A = 9$ isospin quartet," *Physical Review C*, vol. 10, no. 6, p. 2633, 1974.

[30] R. Sherr and G. Bertsch, "Coulomb energy systematics and the missing $j^\pi = (1/2)+$ state in ^{9}B," *Physical Review C*, vol. 32, no. 6, p. 1809, 1985.

[31] M. Fujishiro, T. Tabata, K. Okamoto, and T. Tsujimoto, "Cross section of the reaction ^{9}Be(γ, n) near threshold," *Canadian Journal of Physics*, vol. 60, no. 11, pp. 1672–1677, 1982.

[32] T. Baldwin, *Investigation of the Elusive $\frac{1}{2}^+$ State in ^{9}B*. PhD thesis, University of Surrey, (2006).

[33] R. Sherr and H. Fortune, "Low-lying levels of ^{9}B," *Physical Review C*, vol. 70, no. 5, p. 054312, 2004.

[34] H. Fortune, R. Sherr, and B. Brown, "Coulomb energies in ^{17}Ne and the ground state mass of ^{18}Na," *Physical Review C*, vol. 73, no. 6, p. 064310, 2006.

[35] D. Baye and P. Descouvemont, "Electromagnetic transitions and radiative capture in the generator-coordinate method," *Nuclear Physics A*, vol. 407, no. 1-2, pp. 77–97, 1983.

[36] P. Descouvemont and D. Baye, "Microscopic theory of the ^{8}Be$(\alpha, \gamma)^{12}$C reaction in a three-cluster model," *Physical Review C*, vol. 36, no. 1, p. 54, 1987.

[37] P. Descouvemont, "Microscopic investigation of the $\alpha +^{18}$O system in a three-cluster model," *Physical Review C*, vol. 38, no. 5, 1988.

[38] P. Descouvemont, "^{9}B and ^{9}Be nuclei in a microscopic three-cluster model," *Physical Review C*, vol. 39, no. 4, p. 1557, 1989.

[39] C. Scholl, Y. Fujita, T. Adachi, P. Brentano, H. Fujita, M. Gorska, H. Hoshimoto, H. M. K. K. Hatanaka, T. Nakanishi, Y. Ohta, Y. Sakemi, Y. Shimbara Shimizu, Y. Tameshige, M. Tamii, A. Yosoi, and R. G. T. Zegers, "High resolution study of the ^{9}Be$(^{3}$He$,t)^{9}$B reaction upto the ^{9}B triton threshold," *Physical Review C*, vol. 84, p. 014308, 2011.

[40] E. P. Wigner and L. Eisenbud, "Higher angular momenta and long range interaction in resonance reactions," *Physical Review*, vol. 72, p. 29, 1947.

[41] A. Lane and R. Thomas, "R-matrix theory of nuclear reactions," *Reviews of Modern Physics*, vol. 30, no. 2, p. 257, 1958.

[42] F. Barker and P. Treacy, "Nuclear levels near thresholds," *Nuclear Physics*, vol. 38, pp. 33–49, 1962.

[43] F. Barker, "The first excited state of ^{9}B," *Australian Journal of Physics*, vol. 40, p. 307, 1987.

[44] J. Marion, T. Bonner, and C. Cook, "Study of the Reactions ^{3}T$(p, n)^{3}$He, ^{7}Li$(p, n)^{7}$Be, ^{9}Be$(p, n)^{9}$B, and ^{19}F$(p, n)^{19}$Ne," *Physical Review C*, vol. 100, no. 1, 1995.

[45] J. Marion, "Excited states in ^{10}B," *Physical Review C*, vol. 103, 1956.

[46] J. Marion and J. Levin, "Investigation of the ^{9}Be$(p,n)^9$B and ^{9}Be$(p,\alpha\gamma)^6$Li Reactions," *Physical Review C*, vol. 115, no. 1, 1959.

[47] Y. Saji, "Energy spectrum and angular distributions of neutrons from the reaction ^{9}Be$(p,n)^9$B at 8 to 14 MeV of proton energies," *Journal of the Physical Society of Japan*, vol. 15, no. 3, pp. 367–371, 1960.

[48] G. D. Symons and P. B. Treacy, "Evidence for A 1.7 MeV level in ^{9}B," *Physics Letters*, vol. 2, 1962.

[49] E. Teranishi and B. Furubayashi, "Level width of the ground state of ^{9}B," *Physics Letters*, vol. 9, no. 2, pp. 157–159, 1964.

[50] K. Kadija, G. Paic, and B. Antolkovic, "^{9}B excited states and analysis of the ^{9}Be$(^3$He$,t)$ spectra," *Physical Review C*, vol. 36, 1987.

[51] M. Burlein, H. T. Fortune, P. H. Kutt, and R. Gilman, "Energies and widths of states in ^{9}B," *Physical Review C*, vol. 38, 1988.

[52] H. Akimune, M. Fujimura, M. Fujiwara, K. Hara, T. Ishkawa, T. Kawabata, H. Utsunomiya, T. Yamagata, K. Yamasaki, and M. Yosoi, "Evidence for a 3.80 MeV state in ^{9}B," *Physical Review C*, vol. 64, 2001.

[53] C. Wheldon, T. Kokalova, M. Freer, J. Walshe, R. Hertenberger, H. Wirth, N. Ashwood, M. Barr, N. Curtis, T. Faestermann, *et al.*, "Spectroscopy of ^{9}B via high-resolution ejectile-tagged recoil break-up," *Physical Review C*, vol. 91, no. 2, p. 024308, 2015.

[54] R. J. Slobodrian, H. Bichsel, J. S. C. Mckee, and W. F. Tivol, "High-resolution fast-neutron spectroscopy of the reaction ^{9}Be$(p,n)^9$B at 20 MeV," *Physical Review Letters*, vol. 19, no. 10, p. 595, 1967.

[55] J. Anderson, C. Wong, B. Pohl, and J. McClure, "Fast-neutron spectroscopy of the reaction ^{9}Be$(p,n)^9$B at 20 MeV," *Physical Review C*, vol. 2, no. 1, p. 319, 1970.

[56] N. Arena, S. Cavallaro, G. Fazio, G. Giardina, A. Italiano, and F. Mezzanares, "Energy and width measurement of the 9b first excited state observed by the ^{10}B(^{3}He, α)^{9}B(p)^{8}Be and ^{10}B(^{3}He, α)^{9}B(α)^{5}Li reactions," *EPL (Europhysics Letters)*, vol. 5, no. 6, p. 517, 1988.

[57] M. A. Tiede, K. W. Kemper, N. R. Fletcher, D. Robson, D. D. Caussyn, S. fett, J. D. Brown, W. N. Catford, C. Jones, D. Watson, and W. D. M. Rae, "Measurement of low-lying states in ^{9}B," *Physical Review C*, vol. 52, p. 1315, 1995.

[58] T. Baldwin, W. N. Catford, D. A. Mahboub, C. N. A. N. I. Timis, N. M. a. N. Clarke, V. Ziman, T. A. Brown, S. P. Fox, B. R. Fulton, D. Groombridge, D. I. Watson, V. F. Pucknell, and D. C. Weisser, "First excited $\frac{1}{2}^+$ state in ^{9}B," *Physical Review C*, vol. 86, 2012.

[59] K. Li, "Characterization of the pre-eminent $4-\alpha$ cluster state candidate in ^{16}O," Master's thesis, University of Stellenbosch, 2015.

[60] P. Adsley, R. Neveling, P. Papka, Z. Dyers, J. Brümmer, C. Diget, N. Hubbard, K. Li, A. Long, D. Marín Lámbarri, *et al.*, "Cake: The coincidence array for k600 experiments," *Journal of Instrumentation*, vol. 12, no. 02, p. T02004, 2017.

[61] R. Neveling, H. Fujita, F. Smit, T. Adachi, G. Berg, E. Buthelezi, J. Carter, J. Conradie, M. Couder, R. Fearick, *et al.*, "High energy-resolution zero-degree facility for light-ion scattering and reactions at ithemba labs," *Nuclear Instruments and Methods in Physics Research Section A: Accelerators, Spectrometers, Detectors and Associated Equipment*, vol. 654, no. 1, pp. 29–39, 2011.

[62] "https://daq.tlabs.ac.za/software/midas."

[63] "https://root.cern.ch/."

[64] R. Phillips and S. Thornton, "A fortran program for relativistic kinematic calculations in two-body nuclear reactions.," tech. rep., Oak Ridge National Lab., Tenn., 1967.

[65] N. Kheswa, P. Papka, C. Pineda-Vargas, and R. Newman, "Target characterization by pixe, alpha spectrometry and x-ray absorption," *Nuclear Instruments and Methods in Physics Research Section A: Accelerators, Spectrometers, Detectors and Associated Equipment*, vol. 655, no. 1, pp. 85–87, 2011.

[66] "Srim [http://www. srim. org."

[67] F. Nemulodi. PhD thesis, University of Stellenbosch, (2015).

[68] G. Cowan, *Statistical data analysis*. Oxford university press, 1998.

[69] "http://www.physics.umd.edu/enp/jjkelly/allfit/allfit.html."

[70] S. Dixit, W. Bertozzi, T. Buti, J. Finn, F. Hersman, C. Hyde-Wright, M. Hynes, M. Kovash, B. Norum, J. Kelly, *et al.*, "Structure of ^{9}Be from proton scattering at 180 mev," *Physical Review C*, vol. 43, no. 4, p. 1758, 1991.

[71] J. Kelly, W. Bertozzi, T. Buti, J. Finn, F. Hersman, C. Hyde-Wright, M. Hynes, M. Kovash, B. Murdock, B. Norum, *et al.*, "Density dependence in the two-nucleon effective interaction at 135MeV," *Physical Review C*, vol. 39, no. 4, p. 1222, 1989.

[72] E. Kashy, W. Benenson, and J. Nolen Jr, "$A = 9$ isospin quartet," *Physical Review C*, vol. 9, no. 6, p. 2102, 1974.

[73] "N. J. Mukwevho *et al.*, Physical Review C(R), in press."